Recent advances in application of graphitic carbon nitride-based catalysts for degrading organic contaminants in water through advanced oxidation processes beyond photocatalysis: A critical review

Yang Yang, Xin Li, Chengyun Zhou, Weiping Xiong, Guangming Zeng*, Danlian Huang*, Chen Zhang*, Wenjun Wang, Biao Song, Xiang Tang, Xiaopei Li, Hai Guo

College of Environmental Science and Engineering, Hunan University and Key Laboratory of Environmental Biology and Pollution Control (Hunan University), Ministry of Education, Changsha 410082, P. R. China

* Corresponding authors at: College of Environmental Science and Engineering, Hunan University, Changsha, 410082, P. R. China.

E-mail addresses: zgming@hnu.edu.cn (G. Zeng), huangdanlian@hnu.edu.cn (D. Huang) and zhangchen@hnu.edu.cn (C. Zhang).

Abstract

Advanced oxidation processes (AOPs) have attracted much interest in the field of water treatment owing to their high removal efficiency for refractory organic contaminants. Graphitic carbon nitride (g-C_3N_4)-based catalysts with high performance and cost effectiveness are promising heterogeneous catalysts for AOPs. Most research on g-C_3N_4-based catalysts focuses on photocatalytic oxidation, but increasingly researchers are paying attention to the application of g-C_3N_4-based catalysts in other AOPs beyond photocatalysis. This review aims to concisely highlight recent state-of-the-art progress of g-C_3N_4-based catalysts in AOPs beyond photocatalysis. Emphasis is made on the application of g-C_3N_4-based catalysts in three classical AOPs including Fenton-based processes, catalytic ozonation and persulfates activation. The catalytic performance and involved mechanism of g-C_3N_4-based catalysts in these AOPs are discussed in detail. Meanwhile, the effect of water chemistry including pH, water temperature, natural organic matter, inorganic anions and dissolved oxygen on the catalytic performance of g-C_3N_4-based catalysts are summarized. Moreover, the reusability, stability and toxicity of g-C_3N_4-based catalysts in water treatment are also mentioned. Lastly, perspectives on the major challenges and opportunities of g-C_3N_4-based catalysts in these AOPs are proposed for better developments in the future research.

Keywords: Advanced oxidation processes; Carbon nitride; Organic pollutants; Degradation; Water treatment

1. Introduction

With fast growth of industrialization and population, the water contamination caused by organic pollutants is becoming a serious global issue that threatens public health and safety (Li et al., 2020b; Yang et al., 2020b; Yang et al., 2018a). Various synthetic organics (e.g. dyes, pesticides, pharmaceuticals and personal care products (PPCPs), etc.) are discharged into wastewaters and eventually enter natural water bodies (Chen et al., 2020b; Lefebvre and Moletta, 2006; Liu and Wong, 2013; Tian et al., 2020). It is well known that most of these compounds are persistent organic pollutants (POPs), which will threaten the living organisms, including human beings (Brown and Wright, 2016; Muir and Howard, 2006; Song et al., 2018). A variety of physical and biological treatment methods have been employed for the removal of organic pollutants from water, such as adsorption, ultrafiltration and coagulation (Lei et al., 2020a; Xiang et al., 2019; Zhang et al., 2016). However, insufficient capacity to remove trace organic pollutants and possible secondary pollution limit their practical applications. Thus, highly efficient and environmentally friendly treatment processes are required for the removal of residual organic pollutants from water.

Advanced oxidation processes (AOPs) have stimulated great interest from researchers around the world owing to their high efficiency in degrading and even mineralizing organic pollutants from water (Jia et al., 2020; Klavarioti et al., 2009; Tan et al., 2020). Moreover, AOPs are more environmentally friendly than physical and biological treatment processes as they will not release masses of deleterious residues or divert organic pollutants from one phase to another (Oturan and Aaron, 2014; Ye et al., 2019a; Yi et al., 2019). In AOPs, almost all types of organic pollutants can be degraded or mineralized into intermediate products or CO_2 and H_2O. The outstanding activity and versatility of AOPs are originated from the production of highly reactive species such as ·OH, $SO_4^{\cdot -}$, $^1O_2$ and $\cdot O_2^-$, which can efficiently attack the target contaminants leading to their decomposition (Li

et al., 2020c; Wang and Xu, 2012; Yang et al., 2018b). Specifically, AOPs include homogeneous AOPs and heterogeneous AOPs. The heterogeneous AOPs generally utilize solid catalysts in combination with other systems (H_2O_2, O_3, persulfates, light, etc.) to degrade organic pollutants (Lin et al., 2020; Liu et al., 2019; Yuan et al., 2020). Compared with homogeneous catalysts, the main advantage of heterogeneous catalysts is the convenience of catalysts recovery. For practical applications in water decontamination, heterogeneous catalysts must meet some requirements, such as high activity, sustainability as well as physical and chemical stability. Accordingly, many efforts have been paid to the exploitation of efficient and durable heterogeneous catalysts for AOPs.

Graphitic carbon nitride (g-C_3N_4) has recently emerged as promising catalyst in AOPs because of its simple synthesis, low cost and toxicity, unique electronic structure and good stability (He et al., 2019b; Wang et al., 2020c; Zhou et al., 2019). As a metal-free conjugated polymer semiconductor, the relatively narrow bandgap (about 2.7 eV) of g-C_3N_4 endows it with a superior light absorption capacity (Yang et al., 2019d; Zhou et al., 2020a). Besides, the inherent functional groups and vacancies as well as the sp^2 hybridized carbon network are conductive to the generation and migration of delocalized electrons (Wang et al., 2018; Yang et al., 2020a). Meanwhile, g-C_3N_4 possesses a two-dimensional layered structure and six nitrogen lone-pair electrons, which are in favor of the immobilization and dispersion of metal species (Song et al., 2019a; Yang et al., 2019c). Benefiting from these excellent characteristics, g-C_3N_4-based catalysts have been widely applied in AOPs, especially photocatalysis, to degrade organic pollutants from water (Guo et al., 2020a; Wang et al., 2019d; Wang et al., 2020e; Zhang et al., 2020a). And considerable reviews present broad introduction on the application of g-C_3N_4-based catalysts in photocatalytic oxidation (Ding et al., 2017; Hao et al., 2020; Huang et al., 2019a; Mamba and Mishra, 2016; Ong et al., 2016). However, it is hard to achieve deep mineralization for organic pollutants using photocatalysis. Moreover, the changeable weather

and complex photoreactor also restrict the extensive, large-scale and practical applications of photocatalysis (Loeb et al., 2019; Melchionna and Fornasiero, 2020; Wang et al., 2020a). In recent years, some other AOPs based on g-C_3N_4-based catalysts have drawn great attention owing to their superior oxidation ability and operational stability, such as Fenton-based processes, catalytic ozonation and persulfates activation. In these processes, oxidants like H_2O_2, O_3 and persulfates can be activated by g-C_3N_4-based catalysts to generate highly reactive species for the degradation of organic contaminants in water (Fig. 1). Therefore, it is necessary to give a timely review of the progress of g-C_3N_4-based catalysts in those concerned AOPs.

As a state-of-the-art review, the chief objective of this work is to highlight recent advances of g-C_3N_4-based catalysts in AOPs beyond photocatalysis. The catalytic performance and reaction mechanism of g-C_3N_4-based catalysts in three classical AOPs including Fenton-based processes, catalytic ozonation and persulfates activation are discussed. Meanwhile, the effect of water chemistry on the catalytic performance of g-C_3N_4-based catalysts are summarized, such as pH, water temperature, natural organic matter, inorganic anions and dissolved oxygen. Additionally, the reusability, stability and toxicity of g-C_3N_4-based catalysts in water treatment are mentioned. Ultimately, the challenges and opportunities faced by g-C_3N_4-based catalysts in these AOPs are presented.

2. Application of g-C_3N_4-based catalysts in Fenton-based processes

Fenton reaction is recognized as one of the most effective strategy for degrading organic contaminants from water (Deng et al., 2020; Li et al., 2020a; Pignatello et al., 2006). In a typical Fenton reaction, Fe^{2+} catalyzes the decomposition of H_2O_2 to generate ·OH (Eq. (1)) (Khataee et al., 2016). The generated ·OH can quickly destroy the pollutant structure owing to its high oxidation potential. More importantly, the formed Fe^{3+} can be reduced to Fe^{2+} by H_2O_2 through the Fenton-like

reaction (Eq. (2)) (Gholami et al., 2020b), which enables the continuous generation of ·OH. However, the application of conventional Fenton reaction is generally restricted by its inherent shortcomings such as narrow range of working pH, accumulation of Fe-containing sludge and poor reusability. To overcome these problems, numerous heterogeneous Fenton-like catalysts were developed to replace the homogeneous process (Cheng et al., 2018b; Huang et al., 2019b; Li et al., 2019c).

$$Fe^{2+} + H_2O_2 \rightarrow Fe^{3+} + HO^- + \cdot OH \quad (1)$$

$$Fe^{3+} + H_2O_2 \rightleftarrows Fe^{2+} + H^+ + HO_2 \cdot \quad (2)$$

In the past few years, introducing metal species into g-C_3N_4 to construct Fenton-like catalysts for the degradation of organic pollutants in water (Table 1) has attracted great interest because of its excellent characteristics such as efficient catalytic activity, high stability and environmental friendliness. For example, Wang et al. (Wang and Nan, 2020) utilized Fe-doped g-C_3N_4 (Fe-g-C_3N_4) to catalyze the decomposition of H_2O_2 for degrading methylene blue (MB). The pyridinic N in g-C_3N_4 was easily bonded with the Fe atoms to form active sites, thus enhancing the catalytic activity. Owing to the presence of abundant active sites of Fe(II)-N_x and Fe(III)-N_x, the Fe-g-C_3N_4 exhibited excellent activity in Fenton-like oxidation, achieving 83.7% removal of total organic carbon (TOC) in 60 min. Moreover, the g-C_3N_4 supported iron oxide (CN@IO) was also reported to be an efficient Fenton-like catalyst for the degradation of ciprofloxacin (CIP) (Ding et al., 2019). Under the experimental conditions, almost all CIP was degraded and 48.5% CIP was mineralized, which was ascribed to the accelerated redox cycle of Fe(III)/Fe(II) by g-C_3N_4. Apart from iron species, some other metal species have also been introduced into g-C_3N_4 to fabricate Fenton-like catalyst. The Cu(I) was incorporated into g-C_3N_4 for the degradation of various organic pollutants (Ma et al., 2019b). During the formation of g-C_3N_4, the Cu(II) could be reduced by the released carbon and nitride fragments to form Cu(I), which would be conductive to the enhancement of Fenton-like activity. The

removal efficiencies of Rhodamine B (RhB), Acid Red 73 (AR 73), bisphenol A (BPA) and tetracycline (TC) were 99.2%, 96.0%, 94.6% and 84.4%, respectively, indicating that the Cu(I)-doped g-C_3N_4 (Cu(I)-g-C_3N_4) was an effective Fenton-like catalyst to degrade different kinds of organic pollutants. In addition, Ge et al. (Ge et al., 2018) combined the MgO with g-C_3N_4 to activate H_2O_2 for the degradation of organic dyes. The g-C_3N_4/MgO presented outstanding degradation activities for both anionic and cationic dyes, such as methyl orange (MO), MB and RhB. It was found that the Mg-N and C-O bonding between MgO and g-C_3N_4 played a critical role in the degradation reaction via activating H_2O_2 to generate ·OH.

Nevertheless, the content of metals in these g-C_3N_4-based catalysts was relatively low, resulting in the unsatisfactory catalytic performance in Fenton-like oxidation (Bacalho et al., 2017; Luo et al., 2016). And when the metal content increased, it easily aggregated to form large particles, leading to a reduction in the number of catalytic active sites (Teixeira et al., 2018). To effectively improve the activity of g-C_3N_4-based catalysts in Fenton-like oxidation, some g-C_3N_4-based catalysts with high metal content and dispersion were developed. For example, Zhu et al. (Zhu et al., 2019) synthesized Cu-doped g-C_3N_4 (Cu-g-C_3N_4) with high content of Cu-N_x species by calcining the precursor of melamine templated crystalline copper chloride. In the optimal Cu-g-C_3N_4 composite, the Cu content was up to 25.9 wt % and the Cu was uniformly dispersed in the g-C_3N_4 matrix. The presence of abundant Cu-N_x species could accelerate the decomposition of H_2O_2 to form ·OH. Therefore, the Cu-g-C_3N_4 presented superior catalytic activities for the degradation of RhB, MO and MB. Moreover, decorating g-C_3N_4 with metals in forms of ultra-small clusters and single-atoms has drawn much attention due to the high atom-utilization efficiency (Li et al., 2019e). An et al. (An et al., 2018) successfully embedded high-density ultra-small Fe clusters and single-atom Fe sites in g-C_3N_4 (I-FeN_x/g-C_3N_4) by calcining a mixture of Fe-imidazole coordination compound and melamine. The

145 “nitrogen pots” with six nitrogen lone-pair electrons in g-C_3N_4 could efficiently trap and stabilize
146 ultra-small Fe clusters and single-atom Fe sites. As shown in Fig. 2a-d, high-density (18.2 wt %)
147 ultra-small Fe clusters and single-atom Fe sites were uniformly dispersed in the g-C_3N_4 and no iron
148 nanoparticles could be observed. The energy dispersive X-ray spectroscopy images also showed the
149 uniform distribution of C, N and Fe elements (Fig. 2e). The X-ray absorption near-edge structure
150 (XANES) spectra (Fig. 2f) and extended X-ray absorption fine structure (EXAFS) spectra (Fig. 2g)
151 further demonstrated that the Fe-N_x structure was formed. As the Fe(II)-N_x active sites could quickly
152 decompose H_2O_2 to produce ·OH, the I-FeN_x/g-C_3N_4 catalyst exhibited excellent removal efficiency
153 for MB despite no light (Fig. 2h). Additionally, the iron leaching of I-FeN_x/g-C_3N_4 catalyst was 0.69
154 mg L^{-1}, which was much lower than the nano-Fe_3O_4 (2.3 mg L^{-1}) and Fe_3O_4 (9.8 mg L^{-1}) as well as
155 the European Union standard (2 mg L^{-1}) (Khataee et al., 2017; Li et al., 2019b; Xu and Wang, 2012),
156 indicating that the Fe(II)-N_x configurations was stably implanted into g-C_3N_4.

157 Although some achievements have been done on these g-C_3N_4-based Fenton-like catalysts, there
158 are still some inadequacies and need further improvements. Typically, the reduction of the metals
159 anchored on g-C_3N_4 through the oxidation of H_2O_2 is slow, leading to the insufficient redox cycle of
160 the metals. Additionally, in this process, H_2O_2 is finally decomposed into O_2 or $\cdot O_2^-$, which will cause
161 the waste of H_2O_2 (Bokare and Choi, 2014; Lyu et al., 2015). To resolve these problems, the g-C_3N_4-
162 based catalysts with dual reaction centers were developed to enhance the catalytic activity in Fenton-
163 like process. For example, Xu et al. (Xu et al., 2018) constructed a novel Cu-Al_2O_3-g-C_3N_4 catalyst
164 to promote the selective conversion of H_2O_2 to ·OH for enhancing the Fenton-like catalytic activity.
165 In the Cu-Al_2O_3-g-C_3N_4 system, the electron-rich area around Cu was formed because of the higher
166 electronegativity of Cu than Al as well as the Cu-π interactions between Cu and g-C_3N_4. Therefore,
167 the ·OH could be generated by two different electron transfer processes: the one was from the

electron-rich Cu center to H_2O_2 to produce ·OH, and the other was from H_2O to the electron-poor site to form ·OH. Benefiting from the significant increase of ·OH generation, the Cu-Al_2O_3-g-C_3N_4 catalyst exhibited high activities for the degradation of organic pollutants including RhB, BPA, MB, 2,4-dichlorophenoxyacetic acid (2,4-D) and phenytoin sodium (PHT).

Besides, Lyu et al. (Lyu et al., 2018) combined g-C_3N_4 with in situ formed Cu(II) on the surface of $CuAlO_2$ substrate to fabricate a new Fenton-like catalyst. The C-O-Cu bonding bridge on g-C_3N_4-Cu(II)-$CuAlO_2$ could efficiently strengthen the cation-π interaction through the charge transfer. As verified by the density functional theory (DFT) calculations (Fig. 3a and b) and electron paramagnetic resonance (EPR) analysis (Fig. 3c), the dual reaction centers were formed around the Cu and C sites in CN-Cu(II)-$CuAlO_2$, which was ascribed to the cation-π interaction via the C-O-Cu linkage. As depicted in Fig. 3d, the H_2O_2 was efficiently reduced by electrons to ·OH on the electron-rich Cu center. Meanwhile, the electrons on H_2O_2 and pollutants were trapped by the electron-poor C center and then diverted to the electron-rich area through the C-O-Cu linkage. Therefore, the catalytic activity of CN-Cu(II)-$CuAlO_2$ for the degradation of BPA was greatly enhanced compared with that of g-C_3N_4 and $CuAlO_2$. Moreover, the CN-Cu(II)-$CuAlO_2$ also exhibited excellent catalytic activities for the degradation of other refractory pollutants, such as phenol, 2-chlorphenol, ibuprofen and phenytoin, indicating its huge potential in water purification.

To further improve the activity of g-C_3N_4-based catalysts in Fenton-like oxidation, carbonaceous materials with excellent electron transport property and chemical stability were introduced (Ma et al., 2019a; Wang et al., 2019a). For example, the graphitized mesoporous carbon (GMC) was hybridized with Fe-g-C_3N_4 for the degradation of AR 73 (Ma et al., 2017). The GMC not only provided a mesoporous structure for the growth of g-C_3N_4, but also offered a similar sp^2 bonding structure to promote the electron transfer. Benefiting from the accelerated Fe(III)/Fe(II) redox cycle, the Fe-g-

191 C_3N_4/GMC composite showed high activity for AR 73 degradation in the Fenton-like reaction,
192 obtaining 99.2% removal in 40 min. Additionally, enhanced adsorption (10.7%) caused by the
193 introduction of GMC in Fe-g-C_3N_4/GMC composite might also contribute to the accelerated
194 degradation of AR 73. The carbon nanodots (CDs) were also effective in enhancing the catalytic
195 activity of Fe(II)-doped g-C_3N_4 (Fe(II)-g-C_3N_4) in Fenton-like reaction because they could promote
196 the decomposition of H_2O_2 to produce more ·OH (Fang et al., 2019). In the presence of H_2O_2, the
197 CDs/Fe(II)-g-C_3N_4 composite presented superior activity in the Fenton-like system for MB
198 degradation. Quenching experiments and EPR measurements suggested that ·OH and $\cdot O_2^-$ were the
199 main reactive species responsible for the MB degradation, and $\cdot O_2^-$ was originated from the reaction
200 between H_2O_2 and ·OH.

201 The utilization of solar light to construct a photo-Fenton system is also an effective way to
202 enhance the performance of g-C_3N_4-based catalysts as g-C_3N_4-based catalysts can be easily excited
203 by visible light to generate electrons and holes (Li et al., 2016). In this process, the Fe(III)/Fe(II)
204 redox cycle can be greatly accelerated by the photogenerated electrons, thereby facilitating the
205 decomposition of H_2O_2 to ·OH and promoting the degradation of organic pollutants (Herney-Ramirez
206 et al., 2010; Soon and Hameed, 2011). For example, a Fe_2O_3 quantum dots (QDs)/g-C_3N_4 composite
207 was fabricated to catalyze the decomposition of H_2O_2 for degrading *p*-nitrophenol under visible light
208 (Xi et al., 2019). The excellent separation and transfer of photogenerated charges on Fe_2O_3 QDs/g-
209 C_3N_4 could result in the continuous and fast conversion of Fe(III)/Fe(II). Therefore, the activation of
210 H_2O_2 was improved and the degradation rate of *p*-nitrophenol was dramatically enhanced. Moreover,
211 a photo-Fenton-like membrane was assembled for wastewater treatment by using g-C_3N_4 sol and Fe-
212 containing polyoxometalates (Fe-POMs) as precursors (Lan et al., 2019). Owing to the synergistic
213 effect of photocatalysis and Fenton-like reaction, the photo-Fenton-like membrane displayed

outstanding self-catalytic capacity for degrading retained pollutants. Besides, the construction of photo-electro-Fenton-like system based on g-C_3N_4 has also stimulated great research interest (Yue et al., 2018). In this process, the H_2O_2 is in situ generated in the cathode through the two-electron reduction of O_2, and then the H_2O_2 can be activated by the g-C_3N_4-based catalysts to generate ·OH for the degradation of organic pollutants. Recently, a photo-electro-Fenton-like system with WO_3/g-C_3N_4 was fabricated for CIP degradation (Bai et al., 2019). Compared with the photocatalysis system and electro-Fenton-like system, the photo-electro-Fenton-like system showed superior degradation efficiency for CIP and achieved 80.3% mineralization efficiency within 120 min.

In a word, in Fenton-based processes, g-C_3N_4 can act as an excellent support to immobilize metal species, thus improving the catalytic activity and stability of g-C_3N_4-based catalysts. Specifically, the layered structure of g-C_3N_4 is an effective support for loading of the metal species, which can suppress the mobility, improve the dispersion and avoid the aggregation of metal species. Meanwhile, the "nitrogen pots" with six nitrogen lone-pair electrons in g-C_3N_4 are ideal sites for trapping metal species. The general catalytic mechanisms of g-C_3N_4-based catalysts during Fenton-based processes are depicted in Fig. 1. The active metal species on g-C_3N_4-based catalysts can decompose H_2O_2 to generate ·OH, $\cdot O_2^-$ and $^1O_2$, which will lead to the degradation of organic pollutants.

3. Application of g-C_3N_4-based catalysts in catalytic ozonation

As a powerful oxidant, it is well known that O_3 can react with many organic pollutants. However, the oxidation of some organic pollutants by O_3 is relatively slow because of the selectivity of O_3 to organics, leading to the incomplete removal of pollutants or formation of toxic intermediate products (Esplugas et al., 2007; Hubner et al., 2015). In addition, O_3 presents a low mineralization rate for organic pollutants due to the generation and accumulation of some intermediate products that cannot react with O_3, such as aldehydes and carboxylic acids (Nawrocki and Kasprzykhordern, 2010). To

address these issues, some advanced technologies such as O_3/H_2O_2 process and O_3/UV process were developed to activate O_3 (Miklos et al., 2018). Among these, the catalytic ozonation process has stimulated much research interest as it can promote the activation of O_3 to generate reactive oxygen species (ROS) by the addition of some catalysts (Wang and Bai, 2017; Wang and Chen, 2020). Compared with homogeneous catalytic ozonation, heterogeneous catalytic ozonation is greener, more economical and more convenient. Therefore, many efforts have been devoted to developing novel heterogeneous catalysts for catalytic ozonation.

Graphitic carbon nitride-based catalysts have been demonstrated to be effective heterogeneous catalysts in catalytic ozonation for degrading organic pollutants from water (Table 2). Normally, the delocalized electrons and surface oxygen-containing functional groups are responsible for the activity of g-C_3N_4 in catalytic ozonation. Song et al. (Song et al., 2019b) found that the g-C_3N_4 exhibited activity in catalytic ozonation for the degradation of 4-chlorobenzoic acid (*p*-CBA) and benzotriazole (BZA) due to the presence of electron-rich nitrogen vacancies and surface oxygen-containing functional groups (such as hydroxyl group and carbonyl group). Compared with the sole ozonation (apparent rate constant (k_{obs}): 0.069 and 0.057 min^{-1}), the catalytic ozonation by adding g-C_3N_4-Urea presented better activity for *p*-CBA and BZA degradation (k_{obs}: 0.116 and 0.156 min^{-1}). During the reaction, the O_3 captured the delocalized electrons from the electron-rich nitrogen vacancies in g-C_3N_4 to form the $\cdot O_3^-$ (Eq. (3)) and then the $HO_3\cdot$ (Eq. (4)), which rapidly transformed into ·OH (Eq. (5)). Moreover, the O_3 decomposed aromatic rings in organic species to olefins, which subsequently reacted with O_3 to form H_2O_2. Meanwhile, the carbonyl group in g-C_3N_4 also enhanced the H_2O_2 production (Eq. (6)). And the reaction of H_2O_2 and O_3 could generated more ·OH and $\cdot O_2^-$ (Eqs. (7) and (8)). Therefore, the activity of g-C_3N_4 in catalytic ozonation was greatly enhanced. In addition, the doping of O atoms could increase the amount of surface oxygen-containing functional groups and

nitrogen vacancies of g-C_3N_4, thus enhancing the performance catalytic ozonation (Yuan et al., 2019). The degradation efficiency of atrazine (ATZ) through catalytic ozonation over the oxygen functionalized g-C_3N_4 (O@g-C_3N_4) was increased by 29.76% in comparison with the sole ozonation.

$$O_3 + e^- \rightarrow \cdot O_3^- \quad (3)$$

$$\cdot O_3^- + H_2O \rightarrow HO_3 \cdot + OH^- \quad (4)$$

$$HO_3 \cdot \rightarrow O_2 + \cdot OH \quad (5)$$

$$g\text{-}C_3N_4(C=O) + O_3 + H_2O \rightarrow g\text{-}C_3N_4(C-O) + H_2O_2 + O_2 \quad (6)$$

$$H_2O_2 + H_2O \rightarrow HO_2^- + H_3O^+ \quad (7)$$

$$O_3 + H_3O^+ \rightarrow \cdot OH + \cdot O_2^- + O_2 \quad (8)$$

It has been reported that metal species could significantly promote the decomposition of O_3 to produce ROS (Wang and Bai, 2017; Wang et al., 2019b). Accordingly, numerous g-C_3N_4-based metal-containing catalysts have been constructed recently to realize the synergistic effect of g-C_3N_4 and metal species for efficient catalytic ozonation. For example, the ZnO/g-C_3N_4 was found to be highly active in catalytic ozonation and the k_{obs} of ATZ degradation was 2.73 min^{-1}, which was almost 10.5 times higher than that of ozone alone (Yuan et al., 2018a). The enhanced activity was owing to the host-guest interaction between g-C_3N_4 and ZnO, as well as the increased surface area and improved electron transfer ability. *Tert*-butanol (TBA), *p*-benzoquinone (*p*-BQ) and NaN_3 were utilized as ROS scavengers for ·OH, $\cdot O_2^-$ and $^1O_2$, respectively. The degradation efficiency of ATZ in ZnO/g-C_3N_4/O_3 system was greatly inhibited after the addition of ROS scavengers, implying that $\cdot O_2^-$, $^1O_2$ and ·OH were the major reactive species responsible for ATZ degradation. Besides, the g-C_3N_4 could also provide an ideal site to accommodate Ce(III), thus accelerating the formation of surface hydroxyl groups (Xie et al., 2020). As a result, the Ce(III)-doped g-C_3N_4 (Ce(III)-g-C_3N_4) possessed a high catalytic ozonation activity in oxalate degradation, which was ascribed to the synergistic effect of

surface hydroxyl groups and Ce(III) active site.

Moreover, the $LaCoO_3$/g-C_3N_4 exhibited an outstanding activity in catalytic ozonation for the degradation of BZA due to the formation of electron transfer cycle (Zhang et al., 2019b). The electron transfer cycle in $LaCoO_3$/g-C_3N_4, which was induced by the -C-O-Co bonding and nitrogen vacancy, could accelerate the decomposition of O_3 to generate more ·OH, thus promoting the BZA degradation. As shown in Fig. 4a and b, the k_{obs} raised with the increase of the relative content of -C-O-Co bonding and nitrogen vacancy, indicating the positive role of -C-O-Co bonding and nitrogen vacancy in $LaCoO_3$/g-C_3N_4 in catalytic ozonation. The mechanism for $LaCoO_3$/g-C_3N_4 catalytic ozonation was displayed in Fig. 4c. First, the O_3 trapped the single electrons from nitrogen vacancies to generate $\cdot O_3^-$ (Eq. (3)). Meanwhile, the O_3 was decomposed by the C-O-Co bonding to form $\cdot O_2^-$ and $^1O_2$ (Eq. (9)). And the O_3 could react with OH^- to produce $\cdot O_2^-$ and $HO_2\cdot$ (Eq. (10)). Additionally, the O_2 captured the delocalized electrons from electron-rich centers to generate $\cdot O_2^-$ (Eq. (11)). Then, a series of radical chain reactions (Eqs. (4) and (12)) were induced by the $\cdot O_2^-$ and $HO_2\cdot$ to produce ·OH (Eq. (5)). Thus the catalytic ozonation activity of $LaCoO_3$/g-C_3N_4 for BZA degradation was significantly improved.

$$O_3 \xrightarrow{C-O-Co} \cdot O_2^- + {}^1O_2 + O_2 \quad (9)$$

$$O_3 + OH^- \rightarrow \cdot O_2^- + HO_2 \cdot \quad (10)$$

$$O_2 + e^- \rightarrow \cdot O_2^- \quad (11)$$

$$\cdot O_2^- + O_3 \rightarrow \cdot O_3^- + O_2 \quad (12)$$

Furthermore, the g-C_3N_4-based catalysts were also utilized in O_3/H_2O_2 process to promote the formation of ·OH under acidic conditions. In general, the production of ·OH in O_3/H_2O_2 process is limited under acidic conditions as the HO_2^- that can induce free radical chain reactions to generate ·OH is mainly formed under alkaline conditions (Li et al., 2015; Sein et al., 2008). To overcome this

drawback, Guo et al. (Guo et al., 2019) anchored single Mn atoms on g-C_3N_4 (Mn-CN) to accelerate the ·OH formation for the degradation of oxalic acid (OA). As shown in Fig. 5a and b, the Mn-CN catalyst exhibited high activity for OA degradation in the O_3/H_2O_2 process, which was ascribed to the increased yield of ·OH (Fig. 5c). The chronoamperometry curves (Fig. 5d) and EPR measurements (Fig. 5e) suggested that the HO_2· was formed in the interaction between Mn-CN and H_2O_2, and the O_3 could promote the formation of HO_2·. The energy change plot for different steps (Fig. 5f) further confirmed the reaction mechanism. During the reaction (Fig. 5g), the Mn-N_4 site in Mn-CN catalyst adsorbed H_2O_2 to form the HOO-Mn-N_4 species, which then reacted with O_3 to generate HO_2· and $\cdot O_3^-$. $\cdot O_3^-$ would combine with H^+ in acidic solution to generate HO_3 and it rapidly transformed to ·OH. Meanwhile, HO_2· converted to $\cdot O_2^-$, which could also react with O_3 to produce $\cdot O_3^-$. Therefore, the yield of ·OH was increased and the degradation efficiency of OA was significantly enhanced.

The general catalytic mechanisms of g-C_3N_4-based catalysts during catalytic ozonation are presented in Fig. 1. In brief, the delocalized electrons and surface oxygen-containing functional groups on g-C_3N_4 can promote the transformation of O_3 to generate ·OH and $\cdot O_2^-$. Additionally, the immobilized metal species on g-C_3N_4 also can activate O_3 to produce ·OH, $\cdot O_2^-$ and $^1O_2$. Consequently, these generated ROS will accelerate the degradation of organic pollutants.

4. Application of g-C_3N_4-based catalysts in persulfates activation

As an effective and promising technology for the degradation of organic pollutants in water, the AOPs based on persulfates including peroxymonosulfate (PMS, HSO_5^-) or peroxydisulfate (PDS, $S_2O_8^{2-}$) have received increasing attention in recent years (Qin et al., 2020; Yu et al., 2020; Zhou et al., 2020b). Persulfates are strong oxidants and the redox potential for PMS and PDS are 1.82 V and 2.01 V, respectively. Compared with H_2O_2 and O_3, the persulfates is more convenient for storage and transportation because they usually exist as solid power. However, their direct reaction with most

organic pollutants is so slow, which need further activation for practical applications. In previous studies, numerous strategies such as UV, heat, alkali, ultrasound, transition metals and carbon-based catalysts have been utilized for persulfates activation, where reactive radicals (e.g., $SO_4^{\cdot -}$ and ·OH) or nonradical species ($^1O_2$ and surface-bound complexes) are generated for effectively degrading organic pollutants (Liu et al., 2020b; Wang and Wang, 2018). Among these approaches, heterogeneous catalysis has attracted extensive interests due to its less energy consumption, high catalytic activity and outstanding reusability (Wu et al., 2019). Therefore, many efforts have been devoted to exploring heterogeneous catalysts for persulfates activation.

Graphitic carbon nitride-based catalysts have been considered as effective catalysts for activating persulfates to degrade organic pollutants (Table 3). Normally, the catalytic activity of g-C_3N_4 in persulfates activation is originated from the nitrogen- or oxygen-containing functional groups, defective edges and sp^2 hybridized carbon network (Deng et al., 2016; Duan et al., 2015). However, the physicochemical properties of g-C_3N_4 prepared by different precursors and calcination procedures are usually somewhat different, which may affect their activity for the activation of persulfates. Guan et al. (Guan et al., 2020) investigated the influences of different precursors (e.g., melamine, dicyandiamide and urea) and calcination atmosphere (e.g., air and N_2) on the catalytic activity of g-C_3N_4 in PMS activation. As shown in Fig. 6a and b, the obtained g-C_3N_4 catalysts exhibited different catalytic activities for PMS activation to degrade BPA, and the g-C_3N_4 prepared from melamine and calcined in N_2 possessed the best performance. The difference in their catalytic activities was because of the variation in the type and amount of active sites caused by the different preparation procedures. Generally, methanol (MeOH), *p*-BQ and L-histidine (L-his) were used as ROS scavengers for $SO_4^{\cdot -}$ and ·OH, $\cdot O_2^-$, and $^1O_2$, respectively (Gholami et al., 2020a; Xu et al., 2020). The quenching experiments (Fig. 6c) and EPR tests demonstrated that $SO_4^{\cdot -}$ and ·OH rather than $\cdot O_2^-$ or $^1O_2$ were

the major ROS responsible for the degradation of BPA. Meanwhile, the g-C_3N_4 also exhibited effective catalytic activity to degrade phenol, 2,4,6-tribromophenol (2,4,6-TBP), acetaminophen (ACT), sulfamethoxazole (SMX), ibuprofen (IBP) and benzoic acid (BA) via activating PMS (Fig. 6d), further excluding the contribution of surface-bound reactive complexes. Accordingly, the mechanism of PMS activation by g-C_3N_4 was proposed in Fig. 6e. First, PMS was decomposed by the active sites on the surface of g-C_3N_4 via an electron transfer pathway to form $SO_4^{\cdot -}$ (Eq. (13)) and $SO_5^{\cdot -}$ (Eq. (14)). Then the $SO_4^{\cdot -}$ could react with H_2O to generate ·OH (Eq. (15)), while the $SO_5^{\cdot -}$ could self-react to generate $SO_4^{\cdot -}$ (Eq. (16)), resulting in the BPA degradation.

$$HSO_5^- + e^- \rightarrow SO_4^{\cdot -} + OH^- \quad (13)$$

$$HSO_5^- - e^- \rightarrow SO_5^{\cdot -} + H^+ \quad (14)$$

$$SO_4^{\cdot -} + H_2O \rightarrow \cdot OH + H^+ + SO_4^{2-} \quad (15)$$

$$2SO_5^{\cdot -} \rightarrow 2SO_4^{\cdot -} + O_2 \quad (16)$$

However, the catalytic performance of pure g-C_3N_4 in persulfates activation is greatly suppressed by its poor electron transfer capability (Lin et al., 2018b). To improve the electron mobility of g-C_3N_4 for efficiently activating persulfates, Gao et al. (Gao et al., 2018b) prepared O-doped g-C_3N_4 (O-CN) with modulated electronic structure. As displayed in Fig. 7a and b, compared with pure g-C_3N_4, the electronic structure of O-CN was altered due to the substitution of N atoms by O atoms. Because the electronegativity of O atom is higher than that of C atom and N atom, the electrons of C atoms would flow to the O atom, leading to formation of high and low electron density regions around the O atom and C atom, respectively. Consequently, the electron transfer on O-CN would be accelerated, which was confirmed by the electrochemical impedance spectroscopy (EIS) spectra (Fig. 7c). Benefiting from the modulated electronic structure, the O-CN exhibited excellent catalytic activity in PMS activation for the degradation of BPA, CIP and 2-chlorophenol (2-CP). The EPR tests

and quenching experiments (Fig. 7d) indicated that the O-CN could activate PMS to generate $SO_4^{\cdot -}$, ·OH and $^1O_2$, in which $^1O_2$ was the major ROS responsible for BPA degradation. The N_2-saturated experiment and linear sweep voltammetry (LSV) analysis (Fig. 7e) further demonstrated that $^1O_2$ was originated from the PMS oxidation rather than from the conversion of $\cdot O_2^-$. Therefore, the mechanism of PMS activation by O-CN could be proposed, as depicted in Fig. 7f. The one was the PMS oxidation by electron-poor C atoms to form $SO_5^{\cdot -}$, followed by the reaction between $SO_5^{\cdot -}$ and H_2O to generate $^1O_2$. The other was the PMS reduction by the electrons around the electron-rich O atoms to generate $SO_4^{\cdot -}$ and ·OH.

As many metal species can activate persulfates to degrade organic pollutants, it is reasonable to expect that incorporation of metal species could effectively enhance the catalytic performance of g-C_3N_4 towards persulfates activation (Li et al., 2017; Oh et al., 2017; Zhang et al., 2019a). Meanwhile, the unique structure of g-C_3N_4 with two-dimensional layered nanosheets and six nitrogen lone-pair electrons is conductive to the immobilization and dispersion of metal species. Therefore, many efforts have been devoted to incorporating metal species into g-C_3N_4 for enhancing persulfates activation (Nguyen et al., 2019; Qin et al., 2019; Yang et al., 2019a). For example, Xie et al. (Xie et al., 2019) synthesized Co-doped g-C_3N_4 (Co-g-C_3N_4) for PMS activation to degrade monochlorophenols (MCPs) isomers, including 2-CP, 3-chlorophenol (3-CP) and 4-chlorophenol (4-CP). The Co-g-C_3N_4 exhibited superior catalytic activity in PMS activation compared with g-C_3N_4 due to the doping of Co. The Co doping could promote the generation of $SO_4^{\cdot -}$ (Eqs. (17)-(20)), resulting in the improved degradation of MCPs. Meanwhile, the adsorption experiments and quantum chemical calculations demonstrated that the adsorption behavior based on the intermolecular interactions between Co-g-C_3N_4 and MCPs was benefit to the process of MCPs degradation. Fan et al. (Fan et al., 2019) prepared Mn-doped g-C_3N_4 (Mn-g-C_3N_4) to activate PMS for the degradation of ACT. The catalytic

398 performance of g-C_3N_4 was significantly improved by the doping of Mn. Further researches
399 demonstrated that $^1O_2$ rather than $SO_4{\cdot}^-$ or ·OH was the active species responsible for the degradation
400 of ACT. In addition to transition metal species, noble metal species were also introduced into g-C_3N_4
401 (Feng et al., 2018a). Wang et al. (Wang et al., 2017) found that Pd nanoparticles could greatly enhance
402 the performance of g-C_3N_4 in PMS activation to degrade BPA because it could promote the formation
403 of surface-bound radical intermediates.

404 $$\mathrm{Co(II)\text{-}g\text{-}C_3N_4} + \mathrm{HSO_5^-} \rightarrow \mathrm{Co(III)\text{-}g\text{-}C_3N_4} + \mathrm{SO_4^{\cdot -}} + \mathrm{OH^-} \quad (17)$$

405 $$\mathrm{Co(III)\text{-}g\text{-}C_3N_4} + \mathrm{HSO_5^-} \rightarrow \mathrm{Co(II)\text{-}g\text{-}C_3N_4} + \mathrm{SO_5^{\cdot -}} + \mathrm{H^+} \quad (18)$$

406 $$\mathrm{Co(III)\text{-}g\text{-}C_3N_4} + \mathrm{e^-} \rightarrow \mathrm{Co(II)\text{-}g\text{-}C_3N_4} \quad (19)$$

407 $$\mathrm{SO_4^{\cdot -}} + \mathrm{OH^-} \rightarrow \mathrm{SO_4^{2-}} + \cdot\mathrm{OH} \quad (20)$$

408 Interestingly, it has been found that high-valent iron-oxo species (e.g., Fe^{IV}=O and Fe^{V}=O)
409 instead of ROS (e.g., $SO_4{\cdot}^-$, ·OH and $^1O_2$) were responsible for the degradation of organic pollutants
410 in persulfates activation by Fe-g-C_3N_4 (Li et al., 2019a). For example, Feng et al. (Feng et al., 2018b)
411 synthesized Fe(II)-g-C_3N_4 to activate PMS for the degradation of phenol. Compared with g-C_3N_4, the
412 Fe(II)-g-C_3N_4 possessed superior catalytic activity in PMS activation to degrade phenol, which was
413 attributed to the formation of Fe^{IV}=O. The Fe^{IV}=O could rapidly degrade the phenol through electron
414 transfer. Li et al. (Li et al., 2018) employed Fe(III)-doped g-C_3N_4 (Fe(III)-g-C_3N_4) to activate PMS
415 for the degradation of 4-CP. As shown in Fig. 8a, the degradation efficiency of 4-CP increased with
416 the increase of Fe(III) content in Fe(III)-g-C_3N_4. When oxalate and citrate were added, the
417 degradation efficiency of 4-CP was decreased (Fig. 8b and c). These results suggested that the
418 embedded Fe(III) in g-C_3N_4 framework acted as the active sites for 4-CP degradation. Moreover, the
419 EPR test and quenching experiments demonstrated that traditional ROS in persulfates activation (e.g.,
420 $SO_4{\cdot}^-$, ·OH and $^1O_2$) played an insignificant role in degrading 4-CP. However, the degradation

efficiency of 4-CP was suppressed by adding the dimethyl sulfoxide (DMSO) (Fig. 8d), which is a probe compound for high-valent iron-oxo species. The DMSO can be oxidized by the high-valent iron-oxo species to generate the dimethyl sulfone (DMSO2). Accordingly, it could be concluded that the Fe^{V}=O was formed on Fe(III)-g-C_3N_4 in PMS activation, resulting in the 4-CP degradation via nonradical pathway, as described in Fig. 8e.

In comparison with monometallic species, bimetallic species have a better catalytic activity for persulfates activation because of the strengthened synergistic effect of metallic elements and the presence of abundant redox reactions (Chen et al., 2017; Lei et al., 2020b; Lin et al., 2018a). Thus, a series of bimetallic species have been incorporated into g-C_3N_4 to activate persulfates. For example, Pi et al. (Pi et al., 2020) synthesized $CoFeO_2$/g-C_3N_4 to activate PMS for the degradation of levofloxacin (LVF). The $CoFeO_2$/g-C_3N_4 displayed a higher catalytic performance than $CoFeO_2$ in activating PMS to degrade LVF due to the accelerated redox cycles of metal species. During the reaction, Co(II) and Fe(III) activated HSO_5^- to form $SO_4^{\cdot -}$ (Eqs. (21) and (22)), while Fe(II) and Co(III) activated HSO_5^- to form $SO_5^{\cdot -}$ (Eqs. (23) and (24)), resulting in the LVF degradation. Li et al. (Li et al., 2020d) fabricated $FeCo_2S_4$/g-C_3N_4 to degrade SMX through the activation of PMS. Owing to the synergistic effect between $FeCo_2S_4$ and g-C_3N_4, the catalytic activity of $FeCo_2S_4$/g-C_3N_4 was superior to $FeCo_2S_4$, g-C_3N_4 and Co_3S_4/g-C_3N_4. The degradation efficiency of SMX was determined to be 60.1%, 17.8%, 73.9% and 91.9% for $FeCo_2S_4$, g-C_3N_4, Co_3S_4/g-C_3N_4 and $FeCo_2S_4$/g-C_3N_4, respectively. For $FeCo_2S_4$/g-C_3N_4, $^1O_2$ was identified to be the dominant active species responsible for SMX degradation.

$$HSO_5^- + Co(II) \rightarrow Co(III) + SO_4^{\cdot -} + OH^- \quad (21)$$

$$HSO_5^- + Fe(III) \rightarrow Fe(II) + SO_4^{\cdot -} + H^+ \quad (22)$$

$$HSO_5^- + Co(III) \rightarrow Co(II) + SO_5^{\cdot -} + H^+ \quad (23)$$

$$HSO_5^- + Fe(II) \rightarrow Fe(III) + SO_5^{\cdot -} + OH^- \quad (24)$$

Additionally, metal-free materials with high electrical conductivity were employed to accelerate the electron transfer on g-C_3N_4 for enhancing the activation of persulfates (Chen et al., 2018; Guo et al., 2018; Ye et al., 2019b). For example, Wei et al. (Wei et al., 2016) combined g-C_3N_4 with activated carbon (AC) to activate PMS for the degradation of organic pollutants. Compared with g-C_3N_4 and AC, the g-C_3N_4/AC composite exhibited superior catalytic activity in PMS activation to degrade Acid Orange 7 (AO 7), which was ascribed to the synergistic effect between g-C_3N_4 and AC. Firstly, the specific surface area of g-C_3N_4/AC was larger than that of g-C_3N_4, which could provide more active sites and increase the adsorption ability for AO 7. Secondly, the effective interfacial contact between g-C_3N_4 and AC could greatly facilitate the electron transfer on g-C_3N_4. Therefore, both the radical generation ($SO_4^{\cdot -}$ and ·OH) and the nonradical effect in PMS activation were significantly enhanced, resulting in the efficient degradation of organic pollutants. Yao et al. (Yao et al., 2019) introduced covalent organic framework (COF) into g-C_3N_4 to promote PMS activation for the degradation of Orange II. The electron transfer between g-C_3N_4@COF and PMS was boosted, which was attributed to the good balance between nitrogen content and graphitization degree. As a result, the g-C_3N_4@COF showed excellent catalytic activity in PMS activation to degrade Orange II because of the strengthened nonradical pathway induced by boosted electron transfer.

Recently, the combination of photocatalysis and persulfates activation has drawn increasing attention because the synergistic effect between them could significantly improve the catalytic performance (Gao et al., 2017; Wang et al., 2020d; Yang et al., 2019b). Normally, the persulfates can be activated by the photogenerated electrons on g-C_3N_4-based catalysts to generate $SO_4^{\cdot -}$ and ·OH, resulting in the boosted persulfates activation and enhanced organic pollutants degradation. For example, Gao et al. (Gao et al., 2018a) utilized a Co_3O_4 QDs/g-C_3N_4 heterostructure to degrade TC

under visible light in the presence of PMS. Compared to the case without visible light or PMS, the degradation efficiency was greatly enhanced, which was ascribed to the cooperative effect between photocatalysis and persulfates activation. In the study of Li et al. (Li et al., 2019d), the $CuFe_2O_4$/g-C_3N_4 composite exhibited improved catalytic performance on PDS activation under visible light for the degradation of propranolol due to the self-redox cycles of iron and copper in $CuFe_2O_4$ and the accelerated formation of $SO_4^{\cdot-}$. Moreover, our group recently developed a novel carbonyl and carboxyl groups co-modified g-C_3N_4 and employed it for the PMS activation under visible light to degrade chlortetracycline hydrochloride (Guo et al., 2020b). In this system, the photogenerated electrons were gathered around the electron-withdrawing carbonyl and carboxyl groups of g-C_3N_4. The PMS could be quickly activated by these electrons to generate $SO_4^{\cdot-}$ and ·OH, leading to the efficient degradation of chlortetracycline hydrochloride.

The general catalytic mechanisms of g-C_3N_4-based catalysts during persulfates activation are displayed in Fig. 1. In short, the nitrogen- or oxygen-containing functional groups, defective edges, sp^2 hybridized carbon network and photogenerated electrons of g-C_3N_4 can facilitate the decomposition of persulfates to produce $SO_4^{\cdot-}$ and ·OH. Moreover, the loaded metal species on g-C_3N_4 also can activate persulfates to generate $SO_4^{\cdot-}$, ·OH, $\cdot O_2^-$ and $^1O_2$. Especially, the Fe-N complex on Fe-g-C_3N_4 can bound to PMS, resulting in the formation of high-valent iron-oxo species. As a result, these reactive species will promote the degradation of organic pollutants.

5. The effect of water chemistry on catalytic performance

5.1. Effect of pH

Due to the variable pH values of actual wastewater, it is very important to clarify the effect of pH on the performance of g-C_3N_4-based catalysts in AOPs. Normally, the solution pH affects the surface properties of g-C_3N_4-based catalysts, the structural forms of target contaminants and the

decomposition of oxidants (H_2O_2, O_3 and persulfates), thereby influencing the catalytic performance. The pH at point of zero charge (pH_{pzc}) can help determine the effect of pH on the surface charge of the catalyst. When the solution pH is less than pH_{pzc}, the surface of the catalyst is positively charged, and when the solution pH is greater than pH_{pzc}, the surface of the catalyst is negatively charged. For example, the pH_{pzc} of zero-valent zinc immobilized g-C_3N_4 (ZVZ-g-C_3N_4) was determined to be 5.96 (Yuan et al., 2018b). At the initial pH above pH_{pzc}, the surface of the catalyst was negatively charged as [ZVZ-g-C_3N_4]-O^- group. Therefore, the ZVZ-g-C_3N_4 showed superior catalytic ozonation performance on ATZ degradation in the pH range of 7.0-9.0 since O_3 is more likely to react with negatively charged surface (Fig. 9a). In the study of Li et al. (Li et al., 2020d), the pH_{pzc} of $FeCo_2S_4$/g-C_3N_4 was determined to be 5.9. Accordingly, at the initial pH of 3.5 or 5.0 and 6.5, 8.0 or 9.5, the surface charge of $FeCo_2S_4$/g-C_3N_4 was positive and negative, respectively. Because the SMX existed as anionic species in the pH range of 3.5-9.5, the interaction between $FeCo_2S_4$/g-C_3N_4 and SMX was enhanced at the initial pH of 3.5 and 5.0, promoting the degradation of SMX in the presence of PMS.

In addition, the decomposition of oxidants are also influenced by the solution pH. In alkali media, the oxidability of H_2O_2 is weakened because of its decomposition to O_2 and H_2O (Cheng et al., 2018a). The activity of O_3 alone for organic pollutants degradation under acidic conditions is unsatisfactory. However, at high pH, the abundant OH^- can react with O_3 to accelerate the formation of ·OH, thus promoting the degradation of organic pollutants (Nawrocki and Kasprzykhordern, 2010; Wang and Chen, 2020). Moreover, the PMS will decomposed to SO_4^{2-}, O_2 and H_2O at high pH, inhibiting the generation of ROS (Ball and Edwards, 1956). As shown in Fig. 9b, in the g-C_3N_4/PMS system, the k_{obs} of BPA degradation increased with pH increasing from 5.0 to 7.0, and then decreased as pH further increased to 9.0 (Guan et al., 2020). This phenomenon could be ascribed to the following reasons. At lower pH values, the electron transfer from g-C_3N_4 surface to PMS was inhibited.

513 Moreover, the alkaline conditions weakened the interaction between g-C_3N_4 surface and HSO_5^- and
514 accelerated the self-decomposition of PMS.

515 Nonetheless, most of the g-C_3N_4-based catalysts were applicable in a wide pH range for the
516 degradation of organic pollutants. For example, Gao et al. (Gao et al., 2018b) reported that PMS could
517 be activated by O-CN in a wide pH range of 3.0-9.0 to efficiently degrade BPA (Fig. 9c). The ZnO/g-
518 C_3N_4 exhibited excellent activity in a wide pH range of 3.5-9.5 for ATZ degradation in catalytic
519 ozonation (Yuan et al., 2018a). The degradation efficiency of ATZ at each pH value was all over 95.5%
520 within 3 min, indicating the slight effect of solution pH on the ATZ degradation. Normally, the
521 classical Fenton reaction only works better under acidic conditions because it easily forms iron
522 precipitates under neutral and alkaline conditions. Compared to recent novel heterogeneous Fenton-
523 like catalysts such as Fe-Pd@C (He et al., 2019a) and nFe$_2O_3$/MIL-53(Cu) (Ren et al., 2020), which
524 only worked in a narrow pH range of 3.0-6.0, the g-C_3N_4-based catalysts usually performed well in a
525 wider pH range. For example, in the study of Lyu et al. (Lyu et al., 2018), the CN-Cu(II)-$CuAlO_2$
526 catalyst exhibited effective activity for BPA degradation in a wide pH range of 5.0-9.0, and possessed
527 the highest activity under the neutral conditions. No significant variation in the removal efficiency of
528 BPA could be observed in the pH range of 5.0-7.0 with the change of initial pH. And although the
529 removal efficiency of BPA slightly decreased with the increase of initial pH in the pH range of 7.0-
530 9.0, it could still achieve 70% at pH 9.0 after 120 min reaction, which was attributed to its dual
531 reaction centers. Moreover, the Cu(I)-g-C_3N_4 also displayed satisfactory activity for the degradation
532 of RhB in a wide pH range of 5.0-11.0 (Ma et al., 2019b). Unlike traditional Fenton-like reactions,
533 the removal efficiency of RhB increased with the increase of solution pH in the pH range of 3.0-6.0,
534 while remained almost unchanged as the pH further increased to 11.0. The efficient activity of Cu(I)-
535 g-C_3N_4 for RhB degradation at higher pH values was ascribed to the $^1O_2$, which was more easily

generated under the alkaline conditions than the acidic conditions.

5.2. Effect of water temperature

At ambient temperature, the g-C_3N_4-based catalysts can perform well in Fenton-based processes, catalytic ozonation and persulfates activation. Slight temperature changes will not obviously affect the performance of g-C_3N_4-based catalysts for degrading organic pollutants through these AOPs. For example, the degradation efficiencies of BPA in the CN-Cu(II)-$CuAlO_2$/H_2O_2 system at 25 ℃, 30 ℃ and 35 ℃ were 90%, 93% and 96%, respectively (Lyu et al., 2018). However, if the water temperature fluctuates greatly, the degradation rate of organic pollutants will also change significantly, especially in persulfates activation because heat is an effective method to activate persulfates. Lin et al. (Lin et al., 2018b) utilized S-doped g-C_3N_4 (S-g-C_3N_4) to activate PDS for the degradation of RhB. As shown in Fig. 9d, the k_{obs} of RhB degradation was increased from 0.005 min^{-1} to 0.014 min^{-1} as the temperature was raised from 20 ℃ to 60 ℃. Moreover, in the $FeCo_2S_4$/g-C_3N_4/PMS system, with the rise of temperature from 10 ℃ to 40 ℃, the degradation effciecny of SMX was remarkably increased from 61.2% to 99.9%, and the k_{obs} of SMX degradation was also increased from 0.059 min^{-1} to 0.294 min^{-1} (Li et al., 2020d).

5.3. Effect of natural organic matter

Natural organic matter (NOM) is a complex mixture of organic substances, which is extensively distributed in ground water, surface water and wastewater. In AOPs, the NOM usually competes with target organic pollutants for ROS, leading to the reduction in degradation efficiency. As a major constituent of NOM, humic acid (HA) can react with O_3, which may depress the performance of catalytic ozonation. In the ZnO/g-C_3N_4/O_3 system, the k_{obs} of ATZ degradation decreased from 1.84 to 0.57 min^{-1} when the HA concentration increased from 1.0 to 10.0 mg L^{-1}, which was ascribed to the competition between HA and ATZ for both O_3 and ROS (Yuan et al., 2018a). However, in the

559 O@g-C_3N_4/O_3 system (Fig. 9e), the production of ·OH was increased owing to the reaction between
560 electron-rich moieties of HA and O_3, resulting in the accelerated ATZ degradation (Yuan et al., 2019).
561 In addition, the NOM can also inhibit the g-C_3N_4-based catalysts to active persulfates because its
562 abundant hydroxyl and carboxyl groups retard the reaction between persulfates and g-C_3N_4-based
563 catalysts to generate reactive species. For example, in the Fe(III)-g-C_3N_4/PMS system, the
564 degradation efficiency of 4-CP declined from 93% to 72% with NOM concentration increasing from
565 1.0 to 20.0 mg L^{-1} (Li et al., 2018). This was mainly because of the delayed reaction between PMS
566 and Fe(III)-g-C_3N_4 caused by NOM as well as the competitive reaction between NOM and 4-CP.
567 *5.4. Effect of inorganic anions*
568 Inorganic anions are also ubiquitous in ground water, surface water and wastewater, which can
569 serve as radical scavengers, resulting in an inhibitory effect on the radical-based degradation of
570 organic pollutants. For example, in the ZVZ-g-C_3N_4/O_2 system, the HCO_3^- obviously suppressed
571 ATZ degradation since the ·OH was scavenged by HCO_3^- (Yuan et al., 2018b). In the g-
572 C_3N_4/$MnFe_2O_4$/PMS system, the triclosan (TCS) degradation was inhibited by the HCO_3^- and low
573 concentration of Cl^-, which was attributed to the formation of less reactive radical species, such as
574 ·HCO_3, ·CO_3^- and ·Cl. While the high concentration of Cl^- could promote the degradation of TCS
575 because of the generation of strong oxidizing species, such as Cl_2 and HOCl (Wang et al., 2019c).
576 Besides, the effect of inorganic anions on organic contaminants degradation in the nonradical
577 dominated process is usually insignificant. In the $FeCo_2S_4$/g-C_3N_4/PMS system, the $^1O_2$ dominated
578 nonradical pathway was determined to be the major process for SMX degradation. Thus, the Cl^-,
579 HCO_3^- and $H_2PO_4^-$ showed unremarkable impact on the degradation of SMX (Li et al., 2020d).
580 Similarly, as exhibited in Fig. 9f, in the O-CN/PMS system with $^1O_2$ as the major ROS, the effect of
581 Cl^-, HCO_3^- and CO_3^{2-} on the degradation of BPA was negligible (Gao et al., 2018b). However, in

PMS activation, some inorganic anions such as $H_2PO_4^-$ (Li et al., 2019a) and F^- (Li et al., 2018) would hinder the formation of high-valent iron-oxo species due to the complexation between inorganic anions and iron species, leading to a slight decline in degradation efficiency.

5.5. Effect of dissolved oxygen

Dissolved oxygen (DO) is one of the essential parameters of water chemistry. It has been found that DO could get involved in the free radical chain reactions, thereby influencing the degradation of organic pollutants (Fang et al., 2013; Lu et al., 2019). Generally, as an electron acceptor, DO can react with one electron of catalysts to form $\cdot O_2^-$, which can be further reduced to H_2O_2 when two protons are present (Nosaka and Nosaka, 2017). Besides, the process of persulfates activation can also be affected by DO (Zhang et al., 2018; Zhu et al., 2018). However, there are limited reports on the effect of DO on the performance of g-C_3N_4-based catalysts in these AOPs. Meanwhile, these reports demonstrated that the effect of DO in the Fenton-based processes and persulfates activation over g-C_3N_4-based catalysts was insignificant. For example, in the CDs/Fe(II)-g-C_3N_4/H_2O_2 system (Fang et al., 2019), there was no obvious change in the degradation efficiency of MB in the absence of O_2. Moreover, in the O-CN/PMS system (Gao et al., 2018b), the BPA degradation was not inhibited after N_2 saturation, implying that the $^1O_2$ was not derived from the DO in reaction solution.

6. Reusability, stability and toxicity

From the view of practical applications, the reusability and stability of g-C_3N_4-based catalysts in these AOPs are vital for the treatment of wastewater. Normally, the g-C_3N_4-based catalysts could still keep good catalytic performance after multiple successive cycles. For example, in Fenton-like oxidation, the catalytic activity of Cu-Al_2O_3-g-C_3N_4 for RhB degradation decreased insignificantly after 7 successive cycles, reaching a removal efficiency of 91% in 60 min (Xu et al., 2018). In catalytic ozonation, the decline of the catalytic performance of CuO/g-C_3N_4 for OA degradation was not

obvious after 5 successive cycles (Liu et al., 2020a). In PMS activation, 90% removal of TCS was obtained over g-C_3N_4/$MnFe_2O_4$ after 5 successive cycles (Wang et al., 2019c). In these cycles at lab-scale, centrifugation recovery and magnetic recovery were usually utilized to recover catalyst powder from the reaction suspension. However, in practical applications, they may be complicated and expensive because of the need to install a large capacity centrifuge or a large electromagnetic system. Recently, catalytic membranes have drawn considerable interest in practical applications due to the simple operation with no need to recover catalyst. Chen et al. (Chen et al., 2020a) fabricated a Mn_3O_4/g-C_3N_4@Polytetrafluoroethylene (PTFE) membrane via a facile vacuum filtration method and used it to activate PMS for 4-CP degradation (Fig. 10a and b). As shown in Fig. 10c, the catalytic performance of Mn_3O_4/g-C_3N_4@PTFE membrane still maintained at high level after 5 successive cycles and was able to remove 80% of 4-CP in 60 min.

The stability of g-C_3N_4-based catalysts in these AOPs was also confirmed by a series of characterizations, such as X-ray diffraction (XRD), X-ray photoelectron spectroscopy (XPS), Fourier transform infrared spectroscopy (FTIR), scanning electron microscopy (SEM) and transmission electron microscopy (TEM). In the study of Ma et al. (Ma et al., 2019b), the XANES spectra and EXAFS spectra showed that the chemical state and coordination structure of the Cu in Cu(I)-g-C_3N_4 had no apparent changes before and after reaction (Fig. 10d and e). The XPS spectra also indicated that the Cu(I) was stably existed in g-C_3N_4 via N coordination after reaction (Fig. 10f). Moreover, it has been reported that g-C_3N_4 was chemically stable toward $\cdot O_2^-$ and O_3 (Xiao et al., 2017). And although ·OH can directly tear the heptazine unit from g-C_3N_4 to generate secondary pollutants, the presence of organic pollutants will hinder the fragmentation of g-C_3N_4. In the study of Song et al. (Song et al., 2019b), the SEM, TEM and atomic force microscopy (AFM) images as well as the XRD and Raman spectra displayed that the morphology, crystal structure and framework of g-C_3N_4 were

only slightly changed after catalytic ozonation, suggesting the high stability of g-C_3N_4. And EPR spectra exhibited that the amount of delocalized electrons in g-C_3N_4 decreased not obviously after catalytic ozonation, further verifying the relative chemical stability of g-C_3N_4. Overall, these results demonstrated the good reusability and stability of g-C_3N_4-based catalysts in these AOPs for the degradation of organic contaminants.

Additionally, the toxicity of g-C_3N_4-based catalysts determines their further practical applications. In general, the toxicity of g-C_3N_4-based materials is closely associated with their structure, morphology, composition and physicochemical properties, such as the surface status, dispersion and hydrophilicity (Chen et al., 2015; Liao et al., 2020). Some investigations have demonstrated that the g-C_3N_4-based materials had low toxicity and good biocompatibility, which could meet the requirements of practical applications. For example, Zhang et al. (Zhang et al., 2013) reported that the ultrathin g-C_3N_4 nanosheets possessed nontoxicity and excellent biocompatibility by assessing the viability of HeLa cells after incubation with the g-C_3N_4 via an MTT (3-(4,5-dimethylthiazol-2-yl)-3,5-diphenyltetrazolium bromide) assay. Even if the concentration of incubated g-C_3N_4 was as high as 600 μg mL^{-1}, there was no distinct decrease in cell viability. Feng et al. (Feng et al., 2016) found that the up-conversion nanoparticles (UCNP)@g-C_3N_4-polyethylene glycol (PEG) composite itself had no obvious toxicity to HeLa cells. In the study of He et al. (He et al., 2020), although the short-lived ROS generated by g-C_3N_4 at a concentration of 50 mg L^{-1} or more under simulated solar light would exert injury to the hatched zebrafish larvae, the presence of NOM in water could diminish the hazardous effect.

7. Conclusions and perspectives

In conclusion, the g-C_3N_4-based catalysts presented excellent catalytic activities in Fenton-based processes, catalytic ozonation and persulfates activation, and could efficiently degrade organic

651 contaminants from water through these AOPs. In Fenton-based processes and catalytic ozonation, the
652 ·OH activated by g-C_3N_4-based catalysts was the major reactive species for degrading organic
653 pollutants. While in persulfates activation, the $SO_4^{\cdot -}$, ·OH, $^1O_2$ and high-valent iron-oxo species were
654 responsible for the degradation of organic pollutants. The effect of water chemistry on catalytic
655 performance indicated that the g-C_3N_4-based catalysts could work in a relatively complex water
656 environment. In addition, most of the g-C_3N_4-based catalysts exhibited excellent reusability and
657 stability in these AOPs for organic contaminants degradation and showed good biocompatibility.
658 Although some achievements have been made, there are still many challenges to utilize g-C_3N_4-based
659 catalysts for the degradation of organic pollutants in water through AOPs beyond photocatalysis.
660 Some points are listed as follows:

661 1. The catalytic activity and stability of g-C_3N_4-based catalysts should be further improved. Despite
662 the high degradation efficiency, there is still much room for improvement in the mineralization
663 rate. Moreover, the stability of some g-C_3N_4-based catalysts is unsatisfactory due to the loss of
664 active sites and the leaching of metal species. Thus, it is significant to optimize the synthetic
665 methods of g-C_3N_4-based catalysts and develop new types of g-C_3N_4-based catalysts with
666 excellent catalytic activity and stability.

667 2. The oxidation mechanism of organic pollutants and the toxicity of reaction intermediates should
668 be deeply investigated. Theoretical calculation based on DFT can provide a method to reveal the
669 most preferentially attacked sites and potential reaction intermediates of target contaminants.
670 Meanwhile, it is necessary to assess the eco-toxicity or human toxicity of these intermediate
671 products as they are even more toxic than their parent compounds in some cases.

672 3. The degradation activity test should be performed in the actual wastewater. Normally, there is a
673 huge difference between the composition of simulated wastewater and actual wastewater, which

makes the removal efficiency obtained in simulated wastewater less persuasive. Therefore, it is recommended to develop g-C_3N_4-based catalysts to target the actual wastewater, which will be beneficial to identify the real challenges in practical applications.

4. The scale of the experiments should be enlarged. To date, most investigations have been executed at the lab-scale using small reactors. To achieve the practical applicability of the g-C_3N_4-based catalysts for organic pollutants degradation, more attention should be devoted in the reactor design and scale-up.

Acknowledgements

This study was financially supported by the Program for the National Natural Science Foundation of China (51521006, 51879101, 51579098, 51779090, 51709101, 51809090, 51278176, 51378190), the Three Gorges Follow-up Research Project (2017HXXY-05), the National Program for Support of Top-Notch Young Professionals of China (2014), the Program for Changjiang Scholars and Innovative Research Team in University (IRT_13R17), Hunan Provincial Science and Technology Plan Project (2018SK20410, 2017SK2243, 2016RS3026), Hunan Provincial Innovation Foundation For Postgraduate (CX20190293), the Natural Science Foundation of Hunan Province, China (Grant Nos. 2019JJ50077), and the Fundamental Research Funds for the Central Universities (531119200086, 531118010114, 531107050978, 541109060031).

References

An, S., Zhang, G., Wang, T., Zhang, W., Li, K., Song, C., Miller, J.T., Miao, S., Wang, J. and Guo, X. 2018. High-density ultra-small clusters and single-atom Fe sites embedded in graphitic carbon nitride (g-C_3N_4) for highly efficient catalytic advanced oxidation processes. ACS Nano 12(9), 9441-9450.

Bai, X., Li, Y., Xie, L., Liu, X., Zhan, S. and Hu, W. 2019. A novel Fe-free photo-electro-Fenton-like system for enhanced ciprofloxacin degradation: bifunctional Z-scheme WO_3/g-C_3N_4. Environ. Sci.-Nano 6(9), 2850-2862.

Ball, D.L. and Edwards, J.O. 1956. The Kinetics and Mechanism of the Decomposition of Caro's Acid. I. J. Am. Chem. Soc. 78(6), 1125-1129.

Bicalho, H.D.A., Lopez, J.L., Binatti, I., Batista, P.F.R., Ardisson, J.D., Resende, R.R. and Lorencon, E. 2017. Facile synthesis of highly dispersed Fe(II)-doped g-C_3N_4 and its application in Fenton-like catalysis. Mol. Catal. 435,

156-165.
Bokare, A.D. and Choi, W. 2014. Review of iron-free Fenton-like systems for activating H_2O_2 in advanced oxidation processes. J. Hazard. Mater. 275, 121-135.
Brown, E.D. and Wright, G.D. 2016. Antibacterial drug discovery in the resistance era. Nature 529(7586), 336-343.
Chen, C., Xie, M., Kong, L., Lu, W., Feng, Z. and Zhan, J. 2020a. Mn_3O_4 nanodots loaded g-C_3N_4 nanosheets for catalytic membrane degradation of organic contaminants. J. Hazard. Mater. 390, 122146.
Chen, C., Zhang, F., Li, C., Lu, J., Cui, S., Liu, H. and Li, W. 2017. A magnetic $CoFe_2O_4$-CNS nanocomposite as an efficient, recyclable catalyst for peroxymonosulfate activation and pollutant degradation. RSC Adv. 7(87), 55020-55025.
Chen, S., Huang, D., Zeng, G., Xue, W., Lei, L., Xu, P., Deng, R., Li, J. and Cheng, M. 2020b. In-situ synthesis of facet-dependent $BiVO_4$/Ag_3PO_4/PANI photocatalyst with enhanced visible-light-induced photocatalytic degradation performance: Synergism of interfacial coupling and hole-transfer. Chem. Eng. J. 382, 122840.
Chen, X., Oh, W. and Lim, T. 2018. Graphene- and CNTs-based carbocatalysts in persulfates activation: Material design and catalytic mechanisms. Chem. Eng. J. 354, 941-976.
Chen, Y., Tan, C., Zhang, H. and Wang, L. 2015. Two-dimensional graphene analogues for biomedical applications. Chem. Soc. Rev. 44(9), 2681-2701.
Cheng, M., Lai, C., Liu, Y., Zeng, G., Huang, D., Zhang, C., Qin, L., Hu, L., Zhou, C. and Xiong, W. 2018a. Metal-organic frameworks for highly efficient heterogeneous Fenton-like catalysis. Coord. Chem. Rev. 368, 80-92.
Cheng, M., Zeng, G., Huang, D., Lai, C., Liu, Y., Zhang, C., Wan, J., Hu, L., Zhou, C. and Xiong, W. 2018b. Efficient degradation of sulfamethazine in simulated and real wastewater at slightly basic pH values using Co-SAM-SCS/H_2O_2 Fenton-like system. Water Res. 138, 7-18.
Deng, R., Luo, H., Huang, D. and Zhang, C. 2020. Biochar-mediated Fenton-like reaction for the degradation of sulfamethazine: Role of environmentally persistent free radicals. Chemosphere 255, 126975.
Ding, F., Yang, D., Tong, Z., Nan, Y., Wang, Y., Zou, X. and Jiang, Z. 2017. Graphitic carbon nitride-based nanocomposites as visible-light driven photocatalysts for environmental purification. Environ. Sci.-Nano 4(7), 1455-1469.
Ding, Q., Lam, F.L.Y. and Hu, X. 2019. Complete degradation of ciprofloxacin over g-C_3N_4-iron oxide composite via heterogeneous dark Fenton reaction. J. Environ. Manage. 244, 23-32.
Dong, H., Wei, M., Li, J., Fang, J., Gao, L., Li, X. and Xu, A. 2016. Catalytic performance of supported g-C_3N_4 on MCM-41 in organic dye degradation with peroxymonosulfate. RSC Adv. 6(75), 70747-70755.
Duan, X., Sun, H., Kang, J., Wang, Y., Indrawirawan, S. and Wang, S. 2015. Insights into heterogeneous catalysis of persulfate activation on dimensional-structured nanocarbons. ACS Catal. 5(8), 4629-4636.
Esplugas, S., Bila, D.M., Krause, L.G.T. and Dezotti, M. 2007. Ozonation and advanced oxidation technologies to remove endocrine disrupting chemicals (EDCs) and pharmaceuticals and personal care products (PPCPs) in water effluents. J. Hazard. Mater. 149(3), 631-642.
Fan, J., Qin, H. and Jiang, S. 2019. Mn-doped g-C_3N_4 composite to activate peroxymonosulfate for acetaminophen degradation: The role of superoxide anion and singlet oxygen. Chem. Eng. J. 359, 723-732.
Fang, G., Dionysiou, D.D., Al-Abed, S.R. and Zhou, D. 2013. Superoxide radical driving the activation of persulfate by magnetite nanoparticles: implications for the degradation of PCBs. Appl. Catal. B: Environ. 129, 325-332.
Fang, L., Liu, Z., Zhou, C., Guo, Y., Feng, Y. and Yang, M. 2019. Degradation mechanism of methylene blue by H_2O_2 and synthesized carbon nanodots/graphitic carbon nitride/Fe(II) composite. J. Phys. Chem. C 123(44), 26921-26931.
Feng, L., He, F., Liu, B., Yang, G., Gai, S., Yang, P., Li, C., Dai, Y., Lv, R. and Lin, J. 2016. g-C_3N_4 Coated Upconversion Nanoparticles for 808 nm Near-Infrared Light Triggered Phototherapy and Multiple Imaging. Chem. Mater. 28(21), 7946.

Feng, Y., Li, H., Wu, D., Liao, C., Fan, Y., Lee, P. and Shih, K. 2018a. Supported palladium nanoparticles as highly efficient catalysts for radical production: Support-dependent synergistic effects. Chemosphere 207, 27-32.

Feng, Y., Liao, C., Kong, L., Wu, D., Liu, Y., Lee, P. and Shih, K. 2018b. Facile synthesis of highly reactive and stable Fe-doped g-C_3N_4 composites for peroxymonosulfate activation: A novel nonradical oxidation process. J. Hazard. Mater. 354, 63-71.

Gao, H., Yang, H., Xu, J., Zhang, S. and Li, J. 2018a. Strongly Coupled g-C_3N_4 Nanosheets-Co_3O_4 Quantum Dots as 2D/0D Heterostructure Composite for Peroxymonosulfate Activation. Small 14(31), 1801353.

Gao, Y., Li, S., Li, Y., Yao, L. and Zhang, H. 2017. Accelerated photocatalytic degradation of organic pollutant over metal-organic framework MIL-53(Fe) under visible LED light mediated by persulfate. Appl. Catal. B: Environ. 202, 165-174.

Gao, Y., Zhu, Y., Lyu, L., Zeng, Q., Xing, X. and Hu, C. 2018b. Electronic structure modulation of graphitic carbon nitride by oxygen doping for enhanced catalytic degradation of organic pollutants through peroxymonosulfate activation. Environ. Sci. Technol. 52(24), 14371-14380.

Ge, L., Peng, Z., Wang, W., Tan, F., Wang, X., Su, B., Qiao, X. and Wong, P.K. 2018. g-C_3N_4/MgO nanosheets: light-independent, metal-poisoning-free catalysts for the activation of hydrogen peroxide to degrade organics. J. Mater. Chem. A 6(34), 16421-16429.

Gholami, P., Dinpazhoh, L., Khataee, A., Hassani, A. and Bhatnagar, A. 2020a. Facile hydrothermal synthesis of novel Fe-Cu layered double hydroxide/biochar nanocomposite with enhanced sonocatalytic activity for degradation of cefazolin sodium. J. Hazard. Mater. 381, 120742.

Gholami, P., Khataee, A. and Bhatnagar, A. 2020b. Environmentally superior cleaning of diatom frustules using sono-Fenton process: Facile fabrication of nanoporous silica with homogeneous morphology and controlled size. Ultrason. Sonochem. 64, 105044.

Guan, C., Jiang, J., Pang, S., Chen, X., Webster, R.D. and Lim, T. 2020. Facile synthesis of pure g-C_3N_4 materials for peroxymonosulfate activation to degrade bisphenol A: Effects of precursors and annealing ambience on catalytic oxidation. Chem. Eng. J. 387, 123726.

Guo, F., Lu, J., Liu, Q., Zhang, P., Zhang, A., Cai, Y. and Wang, Q. 2018. Degradation of Acid Orange 7 by peroxymonosulfate activated with the recyclable nanocomposites of g-C_3N_4 modified magnetic carbon. Chemosphere 205, 297-307.

Guo, H., Niu, C., Feng, C., Liang, C., Zhang, L., Wen, X., Yang, Y., Liu, H., Li, L. and Lin, L. 2020a. Steering exciton dissociation and charge migration in green synthetic oxygen-substituted ultrathin porous graphitic carbon nitride for boosted photocatalytic reactive oxygen species generation. Chem. Eng. J. 385, 123919.

Guo, H., Niu, H., Liang, C., Niu, C., Liu, Y., Tang, N., Yang, Y., Liu, H., Yang, Y. and Wang, W. 2020b. Few-layer graphitic carbon nitride nanosheet with controllable functionalization as an effective metal-free activator for peroxymonosulfate photocatalytic activation: Role of the energy band bending. Chem. Eng. J. 401, 126072.

Guo, Z., Xie, Y., Xiao, J., Zhao, Z., Wang, Y., Xu, Z., Zhang, Y., Yin, L., Cao, H. and Gong, J. 2019. Single-atom Mn–N_4 site-catalyzed peroxone reaction for the efficient production of hydroxyl radicals in an acidic solution. J. Am. Chem. Soc. 141(30), 12005-12010.

Hao, Q., Jia, G., Wei, W., Vinu, A., Wang, Y., Arandiyan, H. and Ni, B. 2020. Graphitic carbon nitride with different dimensionalities for energy and environmental applications. Nano Res. 13(1), 18-37.

He, D., Niu, H., He, S., Mao, L., Cai, Y. and Liang, Y. 2019a. Strengthened fenton degradation of phenol catalyzed by core/shell Fe-Pd@C nanocomposites derived from mechanochemically synthesized Fe-Metal organic frameworks. Water Res. 162, 151-160.

He, D., Zhang, C., Zeng, G., Yang, Y., Huang, D., Wang, L. and Wang, H. 2019b. A multifunctional platform by controlling of carbon nitride in the core-shell structure: from design to construction, and catalysis applications. Appl. Catal. B: Environ. 258, 117957.

He, Y., Peng, G., Jiang, Y., Zhao, M., Wang, X., Chen, M. and Lin, S. 2020. Environmental Hazard Potential of Nano-Photocatalysts Determined by Nano-Bio Interactions and Exposure Conditions. Small 16, 1907690.

Herney-Ramirez, J., Vicente, M.A. and Madeira, L.M. 2010. Heterogeneous photo-Fenton oxidation with pillared clay-based catalysts for wastewater treatment: a review. Appl. Catal. B: Environ. 98(1-2), 10-26.

Huang, D., Li, Z., Zeng, G., Zhou, C., Xue, W., Gong, X., Yan, X., Chen, S., Wang, W. and Cheng, M. 2019a. Megamerger in photocatalytic field: 2D g-C_3N_4 nanosheets serve as support of 0D nanomaterials for improving photocatalytic performance. Appl. Catal. B: Environ. 240, 153-173.

Huang, D., Luo, H., Zhang, C., Zeng, G., Lai, C., Cheng, M., Wang, R., Deng, R., Xue, W. and Gong, X. 2019b. Nonnegligible role of biomass types and its compositions on the formation of persistent free radicals in biochar: Insight into the influences on Fenton-like process. Chem. Eng. J. 361, 353-363.

Hubner, U., Von Gunten, U. and Jekel, M. 2015. Evaluation of the persistence of transformation products from ozonation of trace organic compounds - A critical review. Water Res. 68, 150-170.

Jia, M., Yang, Z., Xu, H., Song, P., Xiong, W., Cao, J., Zhang, Y., Xiang, Y., Hu, J. and Zhou, C. 2020. Integrating N and F co-doped TiO_2 nanotubes with ZIF-8 as photoelectrode for enhanced photo-electrocatalytic degradation of sulfamethazine. Chem. Eng. J. 388, 124388.

Khataee, A., Gholami, P. and Vahid, B. 2017. Catalytic performance of hematite nanostructures prepared by N_2 glow discharge plasma in heterogeneous Fenton-like process for acid red 17 degradation. J. Ind. Eng. Chem. 50, 86-95.

Khataee, A., Gholami, P., Vahid, B. and Joo, S.W. 2016. Heterogeneous sono-Fenton process using pyrite nanorods prepared by non-thermal plasma for degradation of an anthraquinone dye. Ultrason. Sonochem. 32, 357-370.

Klavarioti, M., Mantzavinos, D. and Kassinos, D. 2009. Removal of residual pharmaceuticals from aqueous systems by advanced oxidation processes. Environ. Int. 35(2), 402-417.

Lan, H., Wang, F., Lan, M., An, X., Liu, H. and Qu, J. 2019. Hydrogen-bond-mediated self-assembly of carbon-nitride-based photo-Fenton-like membranes for wastewater treatment. Environ. Sci. Technol. 53(12), 6981-6988.

Lefebvre, O. and Moletta, R. 2006. Treatment of organic pollution in industrial saline wastewater: A literature review. Water Res. 40(20), 3671-3682.

Lei, L., Huang, D., Zhang, C., Deng, R., Chen, S. and Li, Z. 2020a. F dopants triggered active sites in bifunctional cobalt sulfide@nickel foam toward electrocatalytic overall water splitting in neutral and alkaline media: Experiments and theoretical calculations. J. Catal. 385, 129-139.

Lei, L., Huang, D., Zhou, C., Chen, S., Yan, X., Li, Z. and Wang, W. 2020b. Demystifying the active roles of NiFe-based oxides/(oxy) hydroxides for electrochemical water splitting under alkaline conditions. Coord. Chem. Rev. 408, 213177.

Li, H., Shan, C. and Pan, B. 2018. Fe(III)-doped g-C_3N_4 mediated peroxymonosulfate activation for selective degradation of phenolic compounds via high-valent iron-oxo species. Environ. Sci. Technol. 52(4), 2197-2205.

Li, H., Shan, C. and Pan, B. 2019a. Development of Fe-doped g-C_3N_4/graphite mediated peroxymonosulfate activation for degradation of aromatic pollutants via nonradical pathway. Sci. Total Environ. 675, 62-72.

Li, J., Fang, J., Gao, L., Zhang, J., Ruan, X., Xu, A. and Li, X. 2017. Graphitic carbon nitride induced activity enhancement of OMS-2 catalyst for pollutants degradation with peroxymonosulfate. Appl. Surf. Sci. 402, 352-359.

Li, J., Li, X., Han, J., Meng, F., Jiang, J., Li, J., Xu, C. and Li, Y. 2019b. Mesoporous bimetallic Fe/Co as highly active heterogeneous Fenton catalyst for the degradation of tetracycline hydrochlorides. Sci Rep 9(1), 15820.

Li, J., Pham, A.N., Dai, R., Wang, Z. and Waite, T.D. 2020a. Recent advances in Cu-Fenton systems for the treatment of industrial wastewaters: Role of Cu complexes and Cu composites. J. Hazard. Mater. 392, 122261.

Li, L., Lai, C., Huang, F., Cheng, M., Zeng, G., Huang, D., Li, B., Liu, S., Zhang, M. and Qin, L. 2019c. Degradation of naphthalene with magnetic bio-char activate hydrogen peroxide: Synergism of bio-char and Fe-Mn binary oxides.

Water Res. 160, 238-248.
Li, R., Cai, M., Xie, Z., Zhang, Q., Zeng, Y., Liu, H., Liu, G. and Lv, W. 2019d. Construction of heterostructured $CuFe_2O_4$/g-C_3N_4 nanocomposite as an efficient visible light photocatalyst with peroxydisulfate for the organic oxidation. Appl. Catal. B: Environ. 244, 974-982.
Li, W., Cao, J., Xiong, W., Yang, Z., Sun, S., Jia, M. and Xu, Z. 2020b. In-situ growing of metal-organic frameworks on three-dimensional iron network as an efficient adsorbent for antibiotics removal. Chem. Eng. J. 392, 124844.
Li, X., Wang, Y., Zhao, J., Wang, H., Wang, B., Huang, J., Deng, S. and Yu, G. 2015. Electro-peroxone treatment of the antidepressant venlafaxine: Operational parameters and mechanism. J. Hazard. Mater. 300, 298-306.
Li, X., Zeng, Z., Zeng, G., Wang, D., Xiao, R., Wang, Y., Zhou, C., Yi, H., Ye, S. and Yang, Y. 2020c. A "bottle-around-ship" like method synthesized yolk-shell Ag_3PO_4@MIL-53(Fe) Z-scheme photocatalysts for enhanced tetracycline removal. J. Colloid Interface Sci. 561, 501-511.
Li, Y., Kong, T. and Shen, S. 2019e. Artificial photosynthesis with polymeric carbon nitride: When meeting metal nanoparticles, single atoms, and molecular complexes. Small 15(32), 1900772.
Li, Y., Li, J., Pan, Y., Xiong, Z., Yao, G., Xie, R. and Lai, B. 2020d. Peroxymonosulfate activation on $FeCo_2S_4$ modified g-C_3N_4 ($FeCo_2S_4$-CN): Mechanism of singlet oxygen evolution for nonradical efficient degradation of sulfamethoxazole. Chem. Eng. J. 384, 123361.
Li, Y., Ouyang, S., Xu, H., Wang, X., Bi, Y., Zhang, Y. and Ye, J. 2016. Constructing solid–gas-interfacial fenton reaction over alkalinized-C_3N_4 photocatalyst to achieve apparent quantum yield of 49% at 420 nm. J. Am. Chem. Soc. 138(40), 13289-13297.
Liao, G., He, F., Li, Q., Zhong, L., Zhao, R., Che, H., Gao, H. and Fang, B. 2020. Emerging graphitic carbon nitride-based materials for biomedical applications. Prog. Mater Sci. 112, 100666.
Lin, K.A., Yang, M., Zhang, Z., Wiafedzi, T. and Lin, Y. 2018a. Prussian Blue analogue supported on sulfur-doped carbon nitride as an enhanced heterogeneous catalyst for activating peroxymonosulfate. J. Colloid Interface Sci. 529, 161-170.
Lin, K.A., Zhang, Z. and Wiafedzi, T. 2018b. Sulfur-doped carbon nitride as a non-metal heterogeneous catalyst for sulfate radical-based advanced oxidation processes in the absence of light irradiation. J. Water Process Eng. 24, 83-89.
Lin, Y., Liu, H., Yang, C., Wu, X., Du, C., Jiang, L. and Zhong, Y. 2020. Gama-graphyne as photogenerated electrons transfer layer enhances photocatalytic performance of silver phosphate. Appl. Catal. B: Environ. 264, 118479.
Liu, J., Li, J., He, S., Sun, L., Yuan, Y. and Xia, D. 2020a. Heterogeneous catalytic ozonation of oxalic acid with an effective catalyst based on copper oxide modified g-C_3N_4. Sep. Purif. Technol. 234, 116120.
Liu, J. and Wong, M.H. 2013. Pharmaceuticals and personal care products (PPCPs): A review on environmental contamination in China. Environ. Int. 59, 208-224.
Liu, S., Lai, C., Li, B., Zhang, C., Zhang, M., Huang, D., Qin, L., Yi, H., Liu, X. and Huang, F. 2020b. Role of radical and non-radical pathway in activating persulfate for degradation of p-nitrophenol by sulfur-doped ordered mesoporous carbon. Chem. Eng. J. 384, 123304.
Liu, Y., Cheng, M., Liu, Z., Zeng, G., Zhong, H., Chen, M., Zhou, C., Xiong, W., Shao, B. and Song, B. 2019. Heterogeneous Fenton-like catalyst for treatment of rhamnolipid-solubilized hexadecane wastewater. Chemosphere 236, 124387.
Loeb, S., Alvarez, P.J.J., Brame, J., Cates, E.L., Choi, W., Crittenden, J.C., Dionysiou, D.D., Li, Q., Lipuma, G. and Quan, X. 2019. The technology horizon for photocatalytic water treatment: sunrise or sunset? Environ. Sci. Technol. 53(6), 2937-2947.
Lu, K., Yang, F., Lin, W., Zhou, S., Xi, T., Song, C. and Kong, Y. 2018. Stabilized pony-sized-$CuFe_2O_4$/carbon nitride porous composites with boosting Fenton-like oxidation activity. ChemistrySelect 3, 4207-4216.
Lu, X., Zhao, J., Wang, Q., Wang, D., Xu, H., Ma, J., Qiu, W. and Hu, T. 2019. Sonolytic degradation of bisphenol S: Effect of dissolved oxygen and peroxydisulfate, oxidation products and acute toxicity. Water Res. 165, 114969.

Luo, L., Zhang, A., Janik, M.J., Song, C. and Guo, X. 2016. Mesoporous graphitic carbon nitride functionalized iron oxides for promoting phenol oxidation activity. RSC Adv. 6(94), 91960-91967.

Lyu, L., Yan, D., Yu, G., Cao, W. and Hu, C. 2018. Efficient destruction of pollutants in water by a dual-reaction-center fenton-like process over carbon nitride compounds-complexed Cu(II)-$CuAlO_2$. Environ. Sci. Technol. 52(7), 4294-4304.

Lyu, L., Zhang, L., He, G., He, H. and Hu, C. 2017. Selective H_2O_2 conversion to hydroxyl radicals in the electron-rich area of hydroxylated C-g-C_3N_4/CuCo–Al_2O_3. J. Mater. Chem. A 5(15), 7153-7164.

Lyu, L., Zhang, L., Wang, Q., Nie, Y. and Hu, C. 2015. Enhanced fenton catalytic efficiency of γ-Cu–Al_2O_3 by σ-Cu^{2+}-ligand complexes from aromatic pollutant degradation. Environ. Sci. Technol. 49(14), 8639-8647.

Ma, J., Huang, Z., Xi, H. and Wen, Y. 2019a. Magnetic Fe-doping g-C_3N_4/graphite: the effect of supporters and the performance in Fenton-like reactions. Desalin. Water Treat. 142, 371-380.

Ma, J., Jia, N., Shen, C., Liu, W. and Wen, Y. 2019b. Stable cuprous active sites in Cu^+-graphitic carbon nitride: Structure analysis and performance in Fenton-like reactions. J. Hazard. Mater. 378, 120782.

Ma, J., Yang, Q., Wen, Y. and Liu, W. 2017. Fe-g-C_3N_4/graphitized mesoporous carbon composite as an effective Fenton-like catalyst in a wide pH range. Appl. Catal. B: Environ. 201, 232-240.

Mamba, G. and Mishra, A.K. 2016. Graphitic carbon nitride (g-C_3N_4) nanocomposites: A new and exciting generation of visible light driven photocatalysts for environmental pollution remediation. Appl. Catal. B: Environ. 198, 347-377.

Melchionna, M. and Fornasiero, P. 2020. Updates on the Roadmap for Photocatalysis. ACS Catal. 10(10), 5493-5501.

Miklos, D., Remy, C., Jekel, M., Linden, K.G., Drewes, J.E. and Hübner, U. 2018. Evaluation of advanced oxidation processes for water and wastewater treatment – A critical review. Water Res. 139, 118-131.

Muir, D.C.G. and Howard, P.H. 2006. Are there other persistent organic pollutants? A challenge for environmental chemists. Environ. Sci. Technol. 40(23), 7157-7166.

Nawrocki, J. and Kasprzykhordern, B. 2010. The efficiency and mechanisms of catalytic ozonation. Appl. Catal. B: Environ. 99(1), 27-42.

Nguyen, T.B., Doong, R., Huang, C.P., Chen, C. and Dong, C. 2019. Activation of persulfate by CoO nanoparticles loaded on 3D mesoporous carbon nitride (CoO@meso-CN) for the degradation of methylene blue (MB). Sci. Total Environ. 675, 531-541.

Nosaka, Y. and Nosaka, A.Y. 2017. Generation and detection of reactive oxygen species in photocatalysis. Chem. Rev. 117(17), 11302-11336.

Oh, W., Chang, V.W.C., Hu, Z., Goei, R. and Lim, T. 2017. Enhancing the catalytic activity of g-C_3N_4 through Me doping (Me = Cu, Co and Fe) for selective sulfathiazole degradation via redox-based advanced oxidation process. Chem. Eng. J. 323, 260-269.

Ong, W., Tan, L., Ng, Y.H., Yong, S.T. and Chai, S. 2016. Graphitic carbon nitride (g-C_3N_4)-based photocatalysts for artificial photosynthesis and environmental remediation: Are we a step closer to achieving sustainability? Chem. Rev. 116(12), 7159-7329.

Oturan, M.A. and Aaron, J. 2014. Advanced oxidation processes in water/wastewater treatment: principles and applications. A review. Crit. Rev. Environ. Sci. Technol. 44(23), 2577-2641.

Pi, Y., Gao, H., Cao, Y., Cao, R., Wang, Y. and Sun, J. 2020. Cobalt ferrite supported on carbon nitride matrix prepared using waste battery materials as a peroxymonosulfate activator for the degradation of levofloxacin hydrochloride. Chem. Eng. J. 379, 122377.

Pignatello, J.J., Oliveros, E. and Mackay, A.A. 2006. Advanced oxidation processes for organic contaminant destruction based on the Fenton reaction and related chemistry. Crit. Rev. Environ. Sci. Technol. 36(1), 1-84.

Qin, F., Peng, Y., Song, G., Fang, Q., Wang, R., Zhang, C., Zeng, G., Huang, D., Lai, C. and Zhou, Y. 2020. Degradation of sulfamethazine by biochar-supported bimetallic oxide/persulfate system in natural water: Performance and

reaction mechanism. J. Hazard. Mater., 122816.
Qin, Q., Gao, X., Wu, X. and Liu, Y. 2019. $NaBH_4$-treated cobalt-doped g-C_3N_4 for enhanced activation of peroxymonosulfate. Mater. Lett. 256, 126623.
Ren, Y., Shi, M., Zhang, W., Dionysiou, D.D., Lu, J., Shan, C., Zhang, Y., Lv, L. and Pan, B. 2020. Enhancing the Fenton-like Catalytic Activity of nFe_2O_3 by MIL-53(Cu) Support: A Mechanistic Investigation. Environ. Sci. Technol. 54(8), 5258-5267.
Sein, M.M., Zedda, M., Tuerk, J., Schmidt, T.C., Golloch, A. and Von Sonntag, C. 2008. Oxidation of diclofenac with ozone in aqueous solution. Environ. Sci. Technol. 42(17), 6656-6662.
Song, B., Xu, P., Zeng, G., Gong, J., Wang, X., Yan, J., Wang, S., Zhang, P., Cao, W. and Ye, S. 2018. Modeling the transport of sodium dodecyl benzene sulfonate in riverine sediment in the presence of multi-walled carbon nanotubes. Water Res. 129, 20-28.
Song, B., Zeng, Z., Zeng, G., Gong, J., Xiao, R., Ye, S., Chen, M., Lai, C., Xu, P. and Tang, X. 2019a. Powerful combination of g-C_3N_4 and LDHs for enhanced photocatalytic performance: A review of strategy, synthesis, and applications. Adv. Colloid Interface Sci., 101999.
Song, Z., Zhang, Y., Liu, C., Xu, B., Qi, F., Yuan, D. and Pu, S. 2019b. Insight into •OH and $•O_2^-$ formation in heterogeneous catalytic ozonation by delocalized electrons and surface oxygen-containing functional groups in layered-structure nanocarbons. Chem. Eng. J. 357, 655-666.
Soon, A.N. and Hameed, B. 2011. Heterogeneous catalytic treatment of synthetic dyes in aqueous media using Fenton and photo-assisted Fenton process. Desalination 269(1-3), 1-16.
Tan, T., Zeng, Z., Zeng, G., Gong, J., Xiao, R., Zhang, P., Song, B., Tang, W. and Ren, X. 2020. Electrochemically enhanced simultaneous degradation of sulfamethoxazole, ciprofloxacin and amoxicillin from aqueous solution by multi-walled carbon nanotube filter. Sep. Purif. Technol. 235, 116167.
Teixeira, I.F., Barbosa, E.C.M., Tsang, S.C. and Camargo, P.H.C. 2018. Carbon nitrides and metal nanoparticles: from controlled synthesis to design principles for improved photocatalysis. Chem. Soc. Rev. 47(20), 7783-7817.
Tian, S., Zhang, C., Huang, D., Wang, R., Zeng, G., Yan, M., Xiong, W., Zhou, C., Cheng, M. and Xue, W. 2020. Recent progress in sustainable technologies for adsorptive and reactive removal of sulfonamides. Chem. Eng. J. 389, 123423.
Wang, D., Saleh, N.B., Sun, W., Park, C.M., Shen, C., Aich, N., Peijnenburg, W.J.G.M., Zhang, W., Jin, Y. and Su, C. 2019a. Next-generation multifunctional carbon-metal nanohybrids for energy and environmental applications. Environ. Sci. Technol. 53(13), 7265-7287.
Wang, J. and Bai, Z. 2017. Fe-based catalysts for heterogeneous catalytic ozonation of emerging contaminants in water and wastewater. Chem. Eng. J. 312, 79-98.
Wang, J. and Chen, H. 2020. Catalytic ozonation for water and wastewater treatment: Recent advances and perspective. Sci. Total Environ. 704, 135249.
Wang, J., Quan, X., Chen, S., Yu, H. and Liu, G. 2019b. Enhanced catalytic ozonation by highly dispersed CeO_2 on carbon nanotubes for mineralization of organic pollutants. J. Hazard. Mater. 368, 621-629.
Wang, J. and Wang, S. 2018. Activation of persulfate (PS) and peroxymonosulfate (PMS) and application for the degradation of emerging contaminants. Chem. Eng. J. 334, 1502-1517.
Wang, J. and Xu, L.J. 2012. Advanced oxidation processes for wastewater treatment: Formation of hydroxyl radical and application. Crit. Rev. Environ. Sci. Technol. 42(3), 251-325.
Wang, J., Yue, M., Han, Y., Xu, X., Yue, Q. and Xu, S. 2019c. Highly-efficient degradation of triclosan attributed to peroxymonosulfate activation by heterogeneous catalyst g-C_3N_4/$MnFe_2O_4$. Chem. Eng. J., 123554.
Wang, L., Zhang, Q., Chen, B., Bu, Y., Chen, Y., Ma, J., Rosario-Ortiz, F.L. and Zhu, R. 2020a. Some issues limiting photo (cata) lysis application in water pollutant control: A critical review from chemistry perspectives. Water Res. 174, 115605.

Wang, S., Liu, Y. and Wang, J. 2020b. Iron and sulfur co-doped graphite carbon nitride (FeO_y/S-g-C_3N_4) for activating peroxymonosulfate to enhance sulfamethoxazole degradation. Chem. Eng. J. 382, 122836.

Wang, W., Niu, Q., Zeng, G., Zhang, C., Huang, D., Shao, B., Zhou, C., Yang, Y., Liu, Y. and Guo, H. 2020c. 1D porous tubular g-C_3N_4 capture black phosphorus quantum dots as 1D/0D metal-free photocatalysts for oxytetracycline hydrochloride degradation and hexavalent chromium reduction. Appl. Catal. B: Environ. 273, 119051.

Wang, W., Wang, H., Li, G., Wong, P.K. and An, T. 2020d. Visible light activation of persulfate by magnetic hydrochar for bacterial inactivation: Efficiency, recyclability and mechanisms. Water Res. 176, 115746.

Wang, W., Xu, P., Chen, M., Zeng, G., Zhang, C., Zhou, C., Yang, Y., Huang, D., Lai, C. and Cheng, M. 2018. Alkali metal-assisted synthesis of graphite carbon nitride with tunable band-gap for enhanced visible-light-driven photocatalytic performance. ACS Sustain. Chem. Eng. 6(11), 15503-15516.

Wang, W., Zeng, Z., Zeng, G., Zhang, C., Xiao, R., Zhou, C., Xiong, W., Yang, Y., Lei, L. and Liu, Y. 2019d. Sulfur doped carbon quantum dots loaded hollow tubular g-C_3N_4 as novel photocatalyst for destruction of Escherichia coli and tetracycline degradation under visible light. Chem. Eng. J. 378, 122132.

Wang, X. and Nan, Z. 2020. Highly efficient Fenton-like catalyst Fe-g-C_3N_4 porous nanosheets formation and catalytic mechanism. Sep. Purif. Technol. 233, 116023.

Wang, Y., Cao, D., Liu, M. and Zhao, X. 2017. Insights into heterogeneous catalytic activation of peroxymonosulfate by Pd/g-C_3N_4: The role of superoxide radical and singlet oxygen. Catal. Commun. 102, 85-88.

Wang, Z., Wang, H., Zeng, Z., Zeng, G., Xu, P., Xiao, R., Huang, D., Chen, X., He, L. and Zhou, C. 2020e. Metal-organic Frameworks derived $Bi_2O_2CO_3$/porous carbon nitride: A nanosized Z-scheme systems with enhanced photocatalytic activity. Appl. Catal. B: Environ. 267, 118700.

Wei, M., Gao, L., Li, J., Fang, J., Cai, W., Li, X. and Xu, A. 2016. Activation of peroxymonosulfate by graphitic carbon nitride loaded on activated carbon for organic pollutants degradation. J. Hazard. Mater. 316, 60-68.

Wu, S., Liu, H., Yang, C., Li, X., Lin, Y., Yin, K., Sun, J., Teng, Q., Du, C. and Zhong, Y. 2019. High-performance porous carbon catalysts doped by iron and nitrogen for degradation of bisphenol F via peroxymonosulfate activation. Chem. Eng. J. 392, 123683.

Xi, J., Xia, H., Ning, X., Zhang, Z., Liu, J., Mu, Z., Zhang, S., Du, P. and Lu, X. 2019. Carbon-Intercalated 0D/2D Hybrid of Hematite Quantum Dots/Graphitic Carbon Nitride Nanosheets as Superior Catalyst for Advanced Oxidation. Small 15(43), 1902744.

Xiao, J., Han, Q., Xie, Y., Yang, J., Su, Q., Chen, Y. and Cao, H. 2017. Is C_3N_4 chemically stable toward reactive oxygen species in sunlight-driven water treatment? Environ. Sci. Technol. 51(22), 13380-13387.

Xie, M., Tang, J., Kong, L., Lu, W., Natarajan, V., Zhu, F. and Zhan, J. 2019. Cobalt doped g-C_3N_4 activation of peroxymonosulfate for monochlorophenols degradation. Chem. Eng. J. 360, 1213-1222.

Xie, Y., Peng, S., Feng, Y. and Wu, D. 2020. Enhanced mineralization of oxalate by highly active and stable Ce(III)-doped g-C_3N_4 catalyzed ozonation. Chemosphere 239, 124612.

Xiong, W., Zeng, Z., Zeng, G., Yang, Z., Xiao, R., Li, X., Cao, J., Zhou, C., Chen, H. and Jia, M. 2019. Metal-organic frameworks derived magnetic carbon-αFe/Fe_3C composites as a highly effective adsorbent for tetracycline removal from aqueous solution. Chem. Eng. J. 374, 91-99.

Xu, H., Ma, R., Zhu, Y., Du, M., Zhang, H. and Jiao, Z. 2020. A systematic study of the antimicrobial mechanisms of cold atmospheric-pressure plasma for water disinfection. Sci. Total Environ. 703, 134965.

Xu, L. and Wang, J. 2012. Fenton-like degradation of 2, 4-dichlorophenol using Fe_3O_4 magnetic nanoparticles. Appl. Catal. B: Environ. 123, 117-126.

Xu, S., Zhu, H., Cao, W., Wen, Z., Wang, J., Francoisxavier, C.P. and Wintgens, T. 2018. Cu-Al_2O_3-g-C_3N_4 and Cu-Al_2O_3-C-dots with dual-reaction centres for simultaneous enhancement of Fenton-like catalytic activity and selective H_2O_2 conversion to hydroxyl radicals. Appl. Catal. B: Environ. 234, 223-233.

Yang, M., Zhang, Z. and Lin, K.A. 2019a. One-step fabrication of cobalt-embedded carbon nitride as a magnetic and

efficient heterogeneous catalyst for activating oxone to degrade pollutants in water. Sep. Purif. Technol. 210, 1-9.

Yang, Q., Ma, Y., Chen, F., Yao, F., Sun, J., Wang, S., Yi, K., Hou, L., Li, X. and Wang, D. 2019b. Recent advances in photo-activated sulfate radical-advanced oxidation process (SR-AOP) for refractory organic pollutants removal in water. Chem. Eng. J. 378, 122149.

Yang, Y., Zeng, G., Huang, D., Zhang, C., He, D., Zhou, C., Wang, W., Xiong, W., Li, X. and Li, B. 2020a. Molecular engineering of polymeric carbon nitride for highly efficient photocatalytic oxytetracycline degradation and H_2O_2 production. Appl. Catal. B: Environ. 272, 118970.

Yang, Y., Zeng, G., Huang, D., Zhang, C., He, D., Zhou, C., Wang, W., Xiong, W., Song, B. and Yi, H. 2020b. In Situ Grown Single-Atom Cobalt on Polymeric Carbon Nitride with Bidentate Ligand for Efficient Photocatalytic Degradation of Refractory Antibiotics. Small, 2001634.

Yang, Y., Zeng, Z., Zeng, G., Huang, D., Xiao, R., Zhang, C., Zhou, C., Xiong, W., Wang, W. and Cheng, M. 2019c. Ti_3C_2 Mxene/porous g-C_3N_4 interfacial Schottky junction for boosting spatial charge separation in photocatalytic H_2O_2 production. Appl. Catal. B: Environ. 258, 117956.

Yang, Y., Zeng, Z., Zhang, C., Huang, D., Zeng, G., Xiao, R., Lai, C., Zhou, C., Guo, H. and Xue, W. 2018a. Construction of iodine vacancy-rich BiOI/Ag@AgI Z-scheme heterojunction photocatalysts for visible-light-driven tetracycline degradation: transformation pathways and mechanism insight. Chem. Eng. J. 349, 808-821.

Yang, Y., Zhang, C., Huang, D., Zeng, G., Huang, J., Lai, C., Zhou, C., Wang, W., Guo, H. and Xue, W. 2019d. Boron nitride quantum dots decorated ultrathin porous g-C_3N_4: intensified exciton dissociation and charge transfer for promoting visible-light-driven molecular oxygen activation. Appl. Catal. B: Environ. 245, 87-99.

Yang, Y., Zhang, C., Lai, C., Zeng, G., Huang, D., Cheng, M., Wang, J., Chen, F., Zhou, C. and Xiong, W. 2018b. BiOX (X= Cl, Br, I) photocatalytic nanomaterials: applications for fuels and environmental management. Adv. Colloid Interface Sci. 254, 76-93.

Yao, Y., Hu, Y., Hu, H., Chen, L., Yu, M., Gao, M. and Wang, S. 2019. Metal-free catalysts of graphitic carbon nitride-covalent organic frameworks for efficient pollutant destruction in water. J. Colloid Interface Sci. 554, 376-387.

Ye, S., Yan, M., Tan, X., Liang, J., Zeng, G., Wu, H., Song, B., Zhou, C., Yang, Y. and Wang, H. 2019a. Facile assembled biochar-based nanocomposite with improved graphitization for efficient photocatalytic activity driven by visible light. Appl. Catal. B: Environ. 250, 78-88.

Ye, S., Zeng, G., Wu, H., Liang, J., Zhang, C., Dai, J., Xiong, W., Song, B., Wu, S. and Yu, J. 2019b. The effects of activated biochar addition on remediation efficiency of co-composting with contaminated wetland soil. Resour. Conserv. Recycl. 140, 278-285.

Yi, H., Yan, M., Huang, D., Zeng, G., Lai, C., Li, M., Huo, X., Qin, L., Liu, S. and Liu, X. 2019. Synergistic effect of artificial enzyme and 2D nano-structured Bi_2WO_6 for eco-friendly and efficient biomimetic photocatalysis. Appl. Catal. B: Environ. 250, 52-62.

Yu, J., Feng, H., Tang, L., Pang, Y., Zeng, G., Lu, Y., Dong, H., Wang, J., Liu, Y. and Feng, C. 2020. Metal-free carbon materials for persulfate-based advanced oxidation process: Microstructure, property and tailoring. Prog. Mater Sci. 111, 100654.

Yuan, S., Wang, M., Liu, J. and Guo, B. 2020. Recent advances of SBA-15-based composites as the heterogeneous catalysts in water decontamination: A mini-review. J. Environ. Manage. 254, 109787.

Yuan, X., Duan, S., Wu, G., Sun, L., Cao, G., Li, D., Xu, H., Li, Q. and Xia, D. 2018a. Enhanced catalytic ozonation performance of highly stabilized mesoporous ZnO doped g-C_3N_4 composite for efficient water decontamination. Appl. Catal. A: Gen. 551, 129-138.

Yuan, X., Qin, W., Lei, X., Sun, L., Li, Q., Li, D., Xu, H. and Xia, D. 2018b. Efficient enhancement of ozonation performance via ZVZ immobilized g-C_3N_4 towards superior oxidation of micropollutants. Chemosphere 205, 369-379.

Yuan, X., Xie, R., Zhang, Q., Sun, L., Long, X. and Xia, D. 2019. Oxygen functionalized graphitic carbon nitride as an efficient metal-free ozonation catalyst for atrazine removal: Performance and mechanism. Sep. Purif. Technol. 211, 823-831.

Yue, D., Qian, X., Kan, M., Fang, M., Jia, J., Yang, X. and Zhao, Y. 2018. A metal-free visible light active photo-electro-Fenton-like cell for organic pollutants degradation. Appl. Catal. B: Environ. 229, 211-217.

Zhang, C., Lai, C., Zeng, G., Huang, D., Yang, C., Wang, Y., Zhou, Y. and Cheng, M. 2016. Efficacy of carbonaceous nanocomposites for sorbing ionizable antibiotic sulfamethazine from aqueous solution. Water Res. 95, 103-112.

Zhang, C., Zhou, Y., Wang, W., Yang, Y., Zhou, C., Wang, L., Lei, L., He, D., Luo, H. and Huang, D. 2020a. Formation of Mo_2C/hollow tubular g-C_3N_4 hybrids with favorable charge transfer channels for excellent visible-light-photocatalytic performance. Appl. Surf. Sci., 146757.

Zhang, M., Yeoh, F., Du, Y. and Lin, K.A. 2019a. Magnetic cobalt-embedded carbon nitride composite derived from one-dimensional coordination polymer as an efficient catalyst for activating oxone to degrade methyltheobromine in water. Sci. Total Environ. 678, 466-475.

Zhang, R., Wang, X., Zhou, L., Liu, Z. and Crump, D. 2018. The impact of dissolved oxygen on sulfate radical-induced oxidation of organic micro-pollutants: a theoretical study. Water Res. 135, 144-154.

Zhang, X., Xie, X., Wang, H., Zhang, J., Pan, B.C. and Xie, Y. 2013. Enhanced Photoresponsive Ultrathin Graphitic-Phase C_3N_4 Nanosheets for Bioimaging. J. Am. Chem. Soc. 135(1), 18-21.

Zhang, X., Zhao, R., Zhang, N., Su, Y., Liu, Z., Gao, R. and Du, C. 2020b. Insight to unprecedented catalytic activity of double-nitrogen defective metal-free catalyst: Key role of coal gangue. Appl. Catal. B: Environ. 263, 118316.

Zhang, Y., Li, Q., Long, Y., Zou, J., Song, Z., Liu, C., Liu, L., Qi, F., Xu, B. and Chen, Z. 2019b. Catalytic ozonation benefit from the enhancement of electron transfer by the coupling of g-C_3N_4 and $LaCoO_3$: Discussion on catalyst fabrication and electron transfer pathway. Appl. Catal. B: Environ. 254, 569-579.

Zhou, C., Zeng, G., Huang, D., Luo, Y., Cheng, M., Liu, Y., Xiong, W., Yang, Y., Song, B. and Wang, W. 2020a. Distorted polymeric carbon nitride via carriers transfer bridges with superior photocatalytic activity for organic pollutants oxidation and hydrogen production under visible light. J. Hazard. Mater. 386, 121947.

Zhou, C., Zeng, Z., Zeng, G., Huang, D., Xiao, R., Cheng, M., Zhang, C., Xiong, W., Lai, C. and Yang, Y. 2019. Visible-light-driven photocatalytic degradation of sulfamethazine by surface engineering of carbon nitride: Properties, degradation pathway and mechanisms. J. Hazard. Mater. 380, 120815.

Zhou, X., Zeng, Z., Zeng, G., Lai, C., Xiao, R., Liu, S., Huang, D., Qin, L., Liu, X. and Li, B. 2020b. Persulfate activation by swine bone char-derived hierarchical porous carbon: multiple mechanism system for organic pollutant degradation in aqueous media. Chem. Eng. J. 383, 123091.

Zhu, C., Zhu, F., Liu, C., Chen, N., Zhou, D., Fang, G. and Gao, J. 2018. Reductive hexachloroethane degradation by $S_2O_8^{\bullet-}$ with thermal activation of persulfate under anaerobic conditions. Environ. Sci. Technol. 52(15), 8548-8557.

Zhu, J., Zhu, X., Cheng, F., Li, P., Wang, F., Xiao, Y. and Xiong, W. 2019. Preparing copper doped carbon nitride from melamine templated crystalline copper chloride for Fenton-like catalysis. Appl. Catal. B: Environ. 256, 117830.

Table 1

Catalytic activity of g-C_3N_4-based catalysts in Fenton-based processes.

Catalyst	Pollutant	Reaction conditions				Catalytic efficiency			Key reactive species	Reference
		[P]	[C]	[H_2O_2]	pH	DE (min)	k_{obs} (min^{-1})	TOC (min)		
Fe-g-C_3N_4	MB	100 mg L^{-1}	0.2 g L^{-1}	199.4 mM	7.21	100% (60)	0.0886	52.5% (60)	·OH, $·O_2^-$	(Wang and Nan, 2020)
CN@IO	CIP	20 mg L^{-1}	1.0 g L^{-1}	5.6 mM	3	100% (60)	-	48.5% (120)	·OH	(Ding et al., 2019)
Fe-g-C_3N_4/GMC	AR 73	50 mg L^{-1}	0.8 g L^{-1}	40 mM	-	99.2% (40)	0.1837	42.9% (40)	·OH	(Ma et al., 2017)
Cu-g-C_3N_4	RhB	10 mg L^{-1}	0.2 g L^{-1}	300 mM	neutral	92.3% (15)	-	42% (60)	·OH, $·O_2^-$, $^1O_2$	(Zhu et al., 2019)
Cu(I)-g-C_3N_4	RhB	50 mg L^{-1}	0.8 g L^{-1}	40 mM	neutral	99.2% (60)	-	22.8% (60)	$^1O_2$, ·OH	(Ma et al., 2019b)
$CuFe_2O_4$-MCN	4-CP	100 mg L^{-1}	1.0 g L^{-1}	2 g L^{-1}	4	100% (60)	0.076	59% (60)	·OH	(Lu et al., 2018)
Cu-Al_2O_3-g-C_3N_4	BPA	20 mg L^{-1}	0.5 g L^{-1}	12.5 mM	7	97.3% (30)	-	72.3% (120)	·OH	(Xu et al., 2018)
OH-CCN/CuCo-Al_2O_3	BPA	0.1 mM	0.8 g L^{-1}	10 mM	7	96.3% (30)	0.11	67.1% (30)	·OH	(Lyu et al., 2017)
CN-Cu(II)-$CuAlO_2$	BPA	25 mg L^{-1}	1.0 g L^{-1}	10 mM	6-7	95.5% (120)	0.027	41.5% (180)	·OH	(Lyu et al., 2018)

[P]: pollutant concentration; [C]: catalyst dosage; [H_2O_2]: H_2O_2 concentration; DE: degradation efficiency; k_{obs}: apparent rate constant; TOC: total organic carbon; MB: methylene blue; CIP: ciprofloxacin; AR 73: Acid Red 73; RhB: Rhodamine B; 4-CP: 4-chlorophenol; BPA: bisphenol A.

Table 2

Catalytic activity of g-C_3N_4-based catalysts in catalytic ozonation.

Catalyst	Pollutant	Reaction conditions				Catalytic efficiency			Key reactive species	Reference
		[P]	[C]	[O_3]	pH	DE (min)	k_{obs} (min^{-1})	TOC (min)		
g-C_3N_4	*p*-CBA	0.084 mM	0.5 g L^{-1}	2 mg L^{-1}	4.75	98% (30)	0.116	60% (30)	·OH, $\cdot O_2^-$	(Song et al., 2019b)
	BZA				6.01	100% (30)	0.156	64% (30)		
O@g-C_3N_4	ATZ	2 mg L^{-1}	0.5 g L^{-1}	5 mg min^{-1}	6	92.91% (5)	0.6279	77.95% (15)	$\cdot O_2^-$, ·OH	(Yuan et al., 2019)
Ce(III)-g-C_3N_4	OA	0.5 mM	0.1 g L^{-1}	6.6 mg min^{-1}	3.5	96.1% (30)	-	90% (30)	·OH	(Xie et al., 2020)
ZVZ-g-C_3N_4	ATZ	2 mg L^{-1}	0.5 g L^{-1}	5 mg min^{-1}	6	96.5% (1.5)	1.852	-	$\cdot O_2^-$, ·OH, $^1O_2$	(Yuan et al., 2018b)
CuO/g-C_3N_4	OA	50 mg L^{-1}	0.5 g L^{-1}	5 mg min^{-1}	6	91% (15)	0.1349	73% (30)	$\cdot O_2^-$, ·OH	(Liu et al., 2020a)
ZnO/g-C_3N_4	ATZ	2 mg L^{-1}	0.5 g L^{-1}	5 mg min^{-1}	6.5	99.5% (2)	2.73	76.8% (15)	$\cdot O_2^-$, ·OH, $^1O_2$	(Yuan et al., 2018a)
$LaCoO_3$/g-C_3N_4	BZA	0.084 mM	0.25 g L^{-1}	1 mg L^{-1}	6.4	90% (30)	0.095	65% (120)	·OH, $^1O_2$, $\cdot O_2^-$	(Zhang et al., 2019b)

[P]: pollutant concentration; [C]: catalyst dosage; [O_3]: O_3 concentration; DE: degradation efficiency; k_{obs}: apparent rate constant; TOC: total organic carbon; *p*-CBA: 4-chlorobenzoic acid; BZA: benzotriazole; ATZ: atrazine; OA: oxalic acid.

Table 3

Catalytic activity of g-C_3N_4-based catalysts in persulfates activation.

Catalyst	Pollutant	Reaction conditions				Catalytic efficiency			Key reactive species	Reference
		[P]	[C]	[PS]	pH	DE (min)	k_{obs} (min^{-1})	TOC (min)		
g-C_3N_4-M	BPA	10 μM	0.5 g L^{-1}	PMS/1 mM	7	100% (40)	0.0982	36.4% (60)	$SO_4^{\cdot-}$, ·OH	(Guan et al., 2020)
O-CN	BPA	0.05 mM	1.0 g L^{-1}	PMS/10 mM	6.4	100% (45)	-	53% (60)	$^1O_2$, ·OH, $SO_4^{\cdot-}$	(Gao et al., 2018b)
g-C_3N_4/AC	AO 7	50 mg L^{-1}	0.2 g L^{-1}	PMS/0.4 g L^{-1}	3.82	96.4% (10)	-	8.2% (10)	·OH, $SO_4^{\cdot-}$	(Wei et al., 2016)
CN-CG	BPA	50 mg L^{-1}	1.0 g L^{-1}	PMS/0.27 mM	7	90% (30)	-	80% (30)	$SO_4^{\cdot-}$, ·OH, $^1O_2$	(Zhang et al., 2020b)
Fe-g-C_3N_4	Phenol	0.1 mM	1.0 g L^{-1}	PMS/5 mM	2.6	100% (20)	~0.32	-	Fe^{IV}=O	(Feng et al., 2018b)
Fe(III)-g-C_3N_4	4-CP	0.1 mM	0.1 g L^{-1}	PMS/1 mM	3	100% (20)	~0.25	-	Fe^{V}=O	(Li et al., 2018)
Co-g-C_3N_4	4-CP	50 mg L^{-1}	1.0 g L^{-1}	PMS/2.5 mM	-	100% (90)	0.062	32% (120)	$SO_4^{\cdot-}$, ·OH	(Xie et al., 2019)
Mn-g-C_3N_4	ACT	20 mg L^{-1}	0.2 g L^{-1}	PMS/0.8 g L^{-1}	6.5	100% (15)	~0.31	-	$^1O_2$, $\cdot O_2^-$	(Fan et al., 2019)
FeO_y/S-g-C_3N_4	SMX	10 mg L^{-1}	0.2 g L^{-1}	PMS/0.8 mM	3.54	100% (90)	0.06	43.9% (90)	$SO_4^{\cdot-}$, ·OH, $^1O_2$	(Wang et al., 2020b)
Mn_3O_4/g-C_3N_4	4-CP	50 mg L^{-1}	0.3 g L^{-1}	PMS/1 mM	-	100% (60)	0.0818	80% (60)	$^1O_2$, $SO_4^{\cdot-}$, ·OH	(Chen et al., 2020a)
$CoFeO_2$/g-C_3N_4	LVF	10 mg L^{-1}	0.1 g L^{-1}	PMS/0.5 mM	3	75% (5)	-	30% (5)	$SO_4^{\cdot-}$	(Pi et al., 2020)
g-C_3N_4/$MnFe_2O_4$	TCS	9 mg L^{-1}	0.2 g L^{-1}	PMS/0.5 mM	11	97% (60)	0.0527	44.6% (60)	$SO_4^{\cdot-}$, ·OH, $\cdot O_2^-$, $^1O_2$	(Wang et al., 2019c)
$FeCo_2S_4$/g-C_3N_4	SMX	19.7 μM	0.02 g L^{-1}	PMS/0.15 mM	6.5	91.9% (15)	0.151	37.1% (15)	$^1O_2$	(Li et al., 2020d)

[P]: pollutant concentration; [C]: catalyst dosage; [PS]: persulfates concentration; DE: degradation efficiency; k_{obs}: apparent rate constant; TOC: total organic carbon; BPA: bisphenol A; AO 7: Acid Orange 7; 4-CP: 4-chlorophenol; ACT: acetaminophen; SMX: sulfamethoxazole; LVF: levofloxacin; TCS: triclosan.

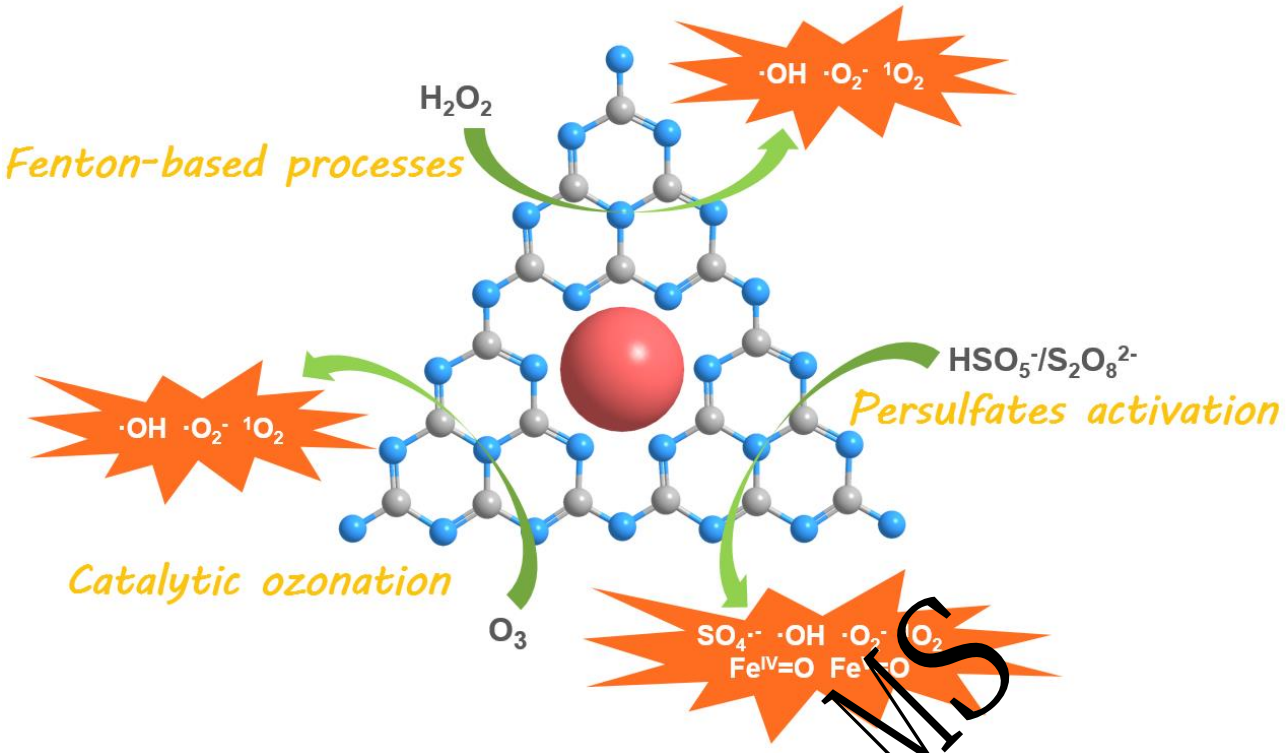

Fig. 1. The catalytic mechanisms of g-C_3N_4-based catalysts for organic contaminants degradation.

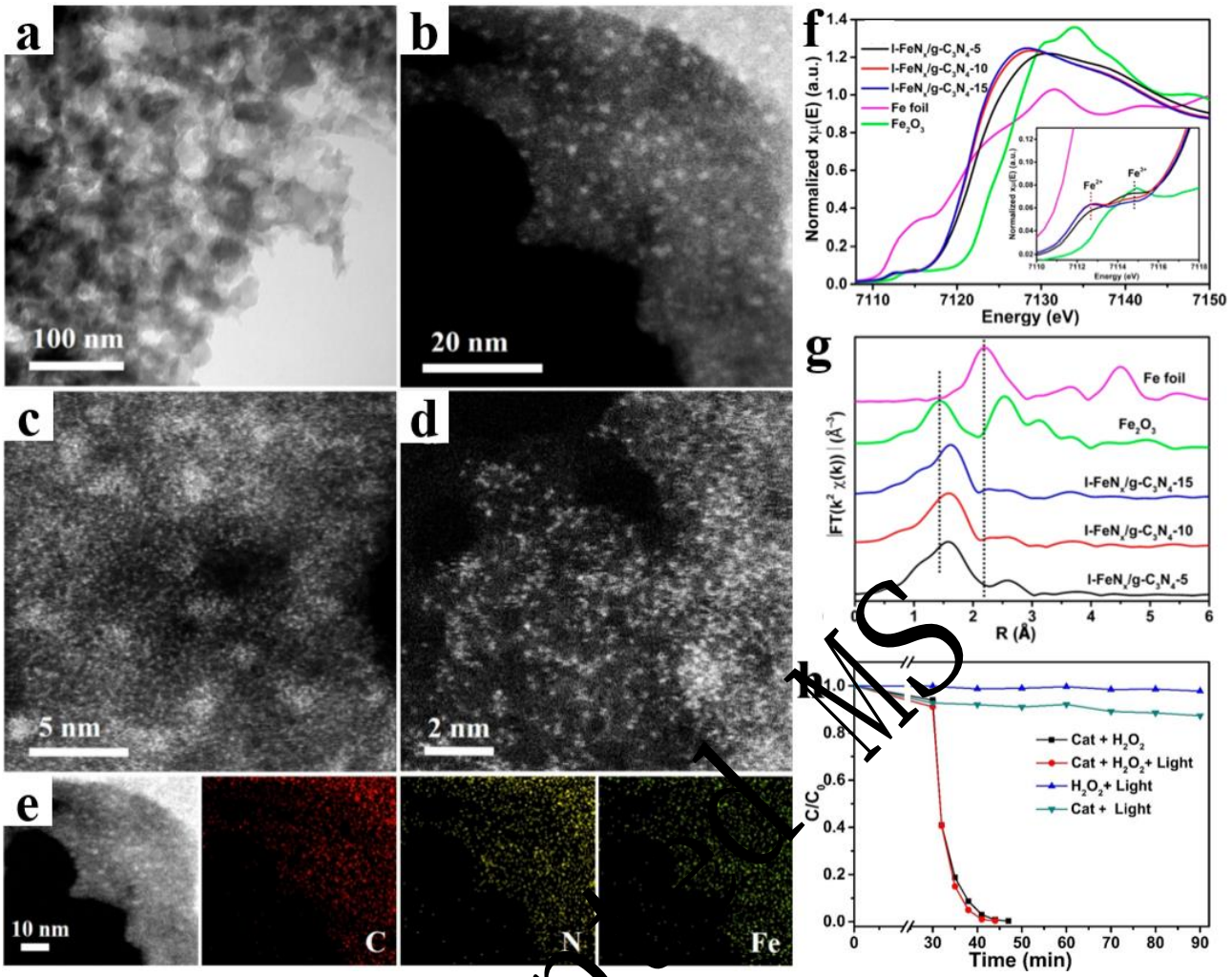

Fig. 2. (a) TEM image, (b-d) HAADF-STEM images and (e) the corresponding element mappings for the C, N, and Fe atoms of I-FeN$_x$/g-C$_3$N$_4$-5 catalyst. (f) K-edge XANES spectra and (g) R-space EXAFS magnitudes of different samples. (h) Removal efficiency of MB using I-FeN$_x$/g-C$_3$N$_4$-5 under various conditions. Reproduced with permission from Ref. (An et al., 2018). Copyright 2018 American Chemical Society.

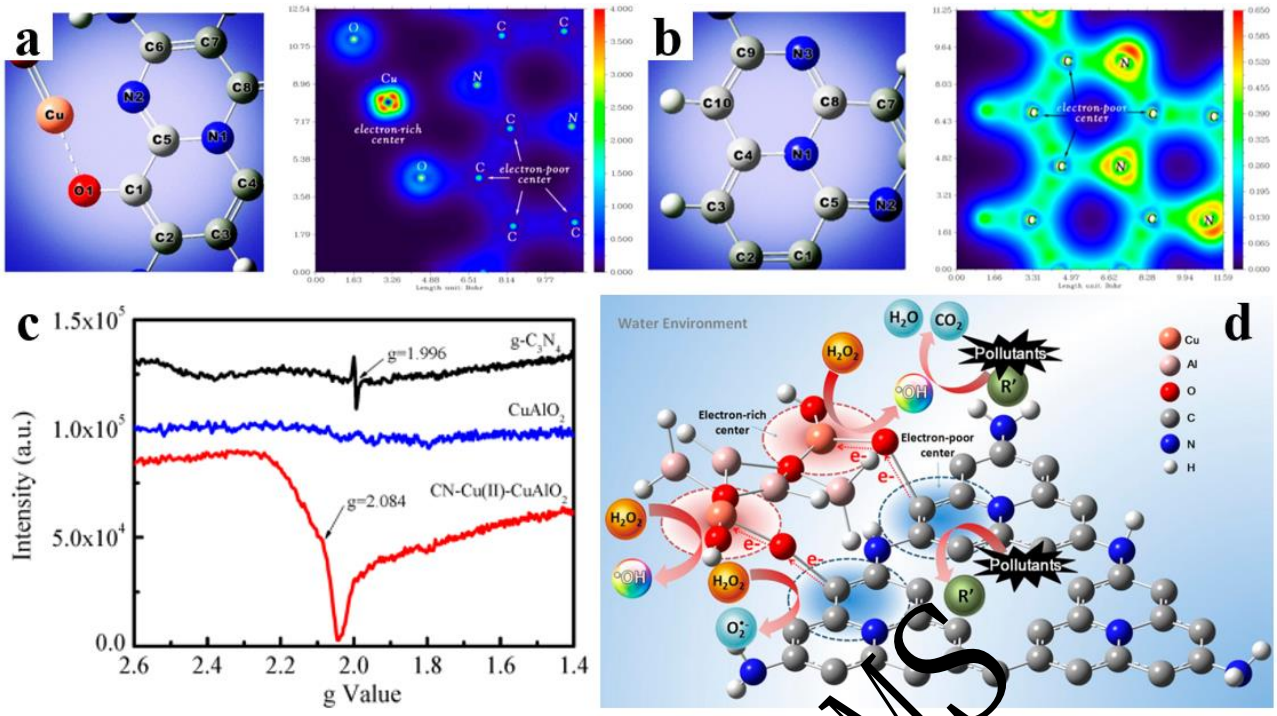

Fig. 3. DFT calculations for the optimized structure and the corresponding two-dimensional valence-electron density color-filled maps of the CN-Cu(II)-$CuAlO_2$ model in (a) Cu(II)-CN vision fragment and (b) -CN vision fragment. (c) EPR spectra of different samples. (d) Fenton-like oxidation mechanism on CN-Cu(II)-$CuAlO_2$. Reproduced with permission from Ref. (Lyu et al., 2018). Copyright 2018 American Chemical Society.

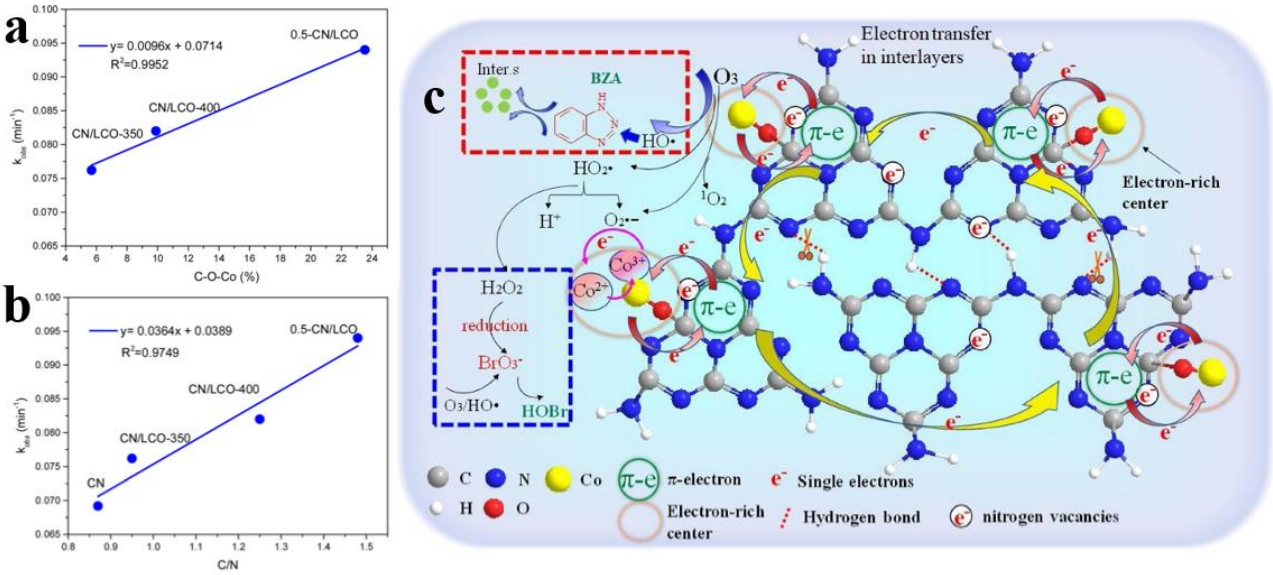

Fig. 4. (a) Effect of -C-O-Co relative content on the degradation efficiency of BZA and (b) effect of C/N on the degradation efficiency of BZA. (c) Reaction mechanism of catalytic ozonation with $LaCoO_3$/g-C_3N_4. Reproduced with permission from Ref. (Zhang et al., 2019b). Copyright 2019 Elsevier.

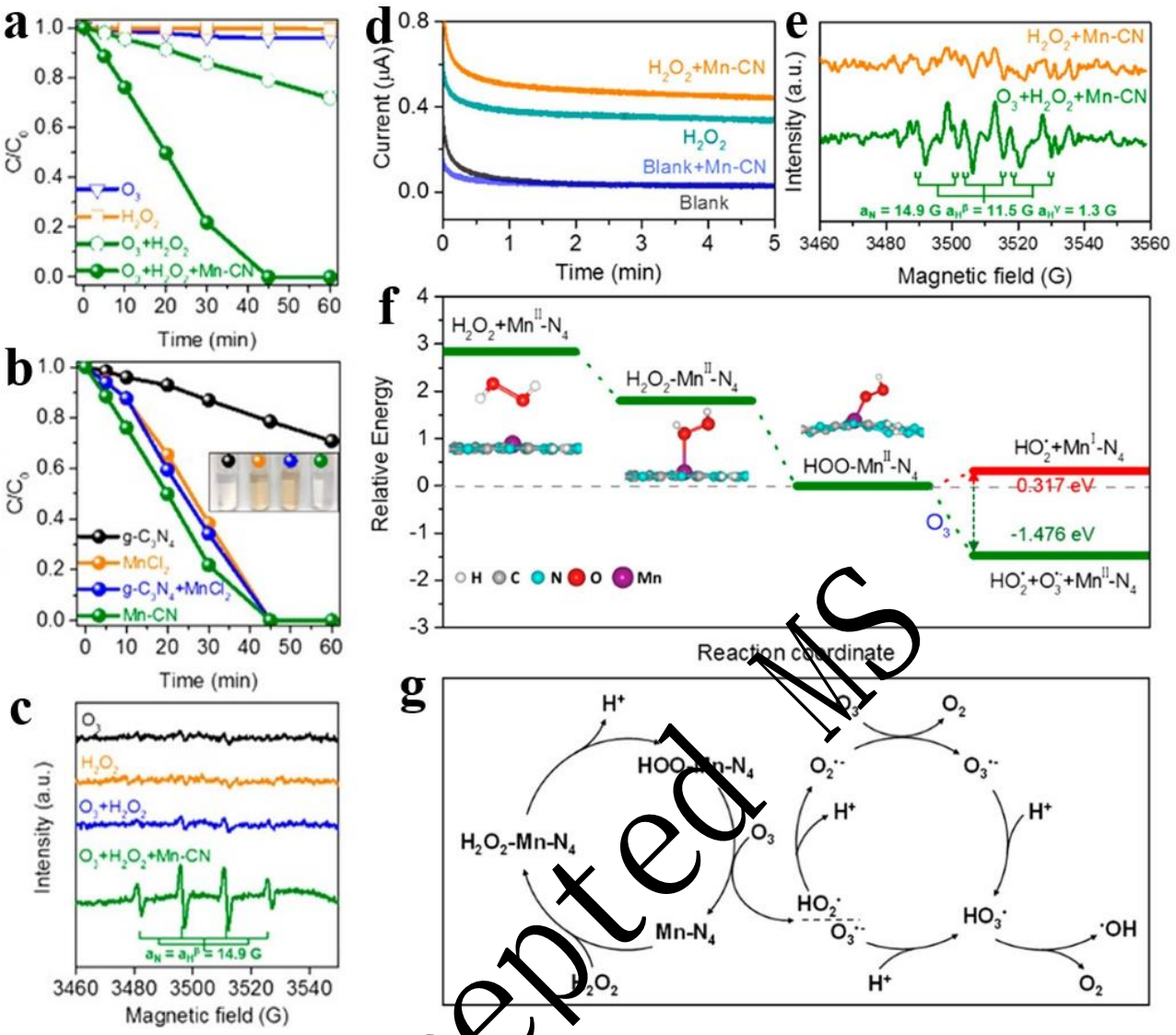

Fig. 5. (a) Degradation curves of OA in ozonation, the H_2O_2 process and the peroxone process with or without Mn-CN. (b) Degradation curves of OA in the peroxone process with g-C_3N_4, $MnCl_2$, a mixture composed of g-C_3N_4 and $MnCl_2$, or Mn-CN. (Inset: Corresponding solution color after reaction.) (c) EPR spectra of the DMPO-·OH adduct in ozonation, the H_2O_2 process, the peroxone process and the peroxone process with Mn-CN. (d) Chronoamperometry curves in blank solution, blank solution with Mn-CN, H_2O_2 solution and H_2O_2 solution with Mn-CN. (e) EPR spectra of the DMPO- HO_2· adduct in the heterogeneous catalytic Fenton process and peroxone reaction with Mn-CN. (f) Free energy of H_2O_2 adsorption and HOO-Mn-N_4 detachment. (g) Reaction mechanism in the Mn-CN catalytic peroxone reaction. Reproduced with permission from Ref. (Guo et al., 2019). Copyright 2019 American Chemical Society.

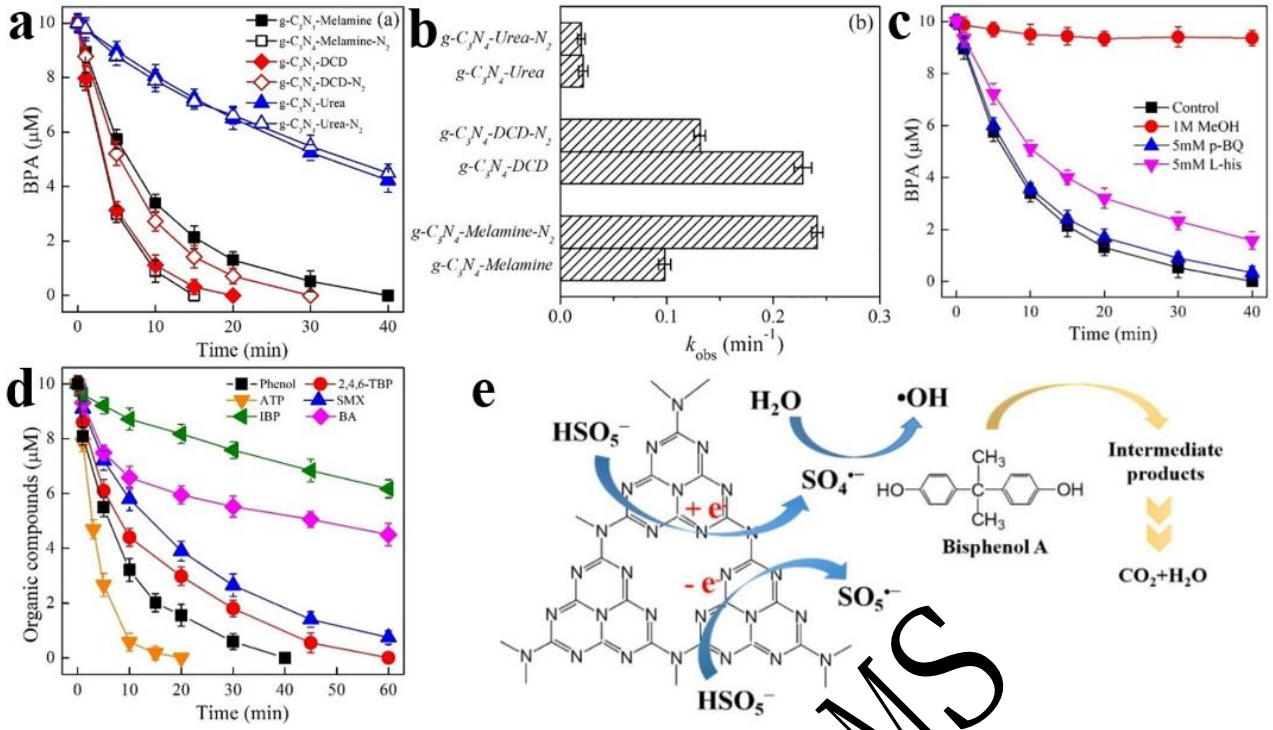

Fig. 6. (a) Time courses of BPA oxidation by PMS in the presence of the as-prepared g-C_3N_4 materials and (b) the k_{obs} for BPA oxidation. (c) Effects of MeOH, *p*-BQ or L-his on degradation of BPA by the g-C_3N_4-Melamine/PMS system. (d) Degradation of various organic compounds by the g-C_3N_4-Melamine/ PMS system. (e) Mechanism of PMS activation by g-C_3N_4. Reproduced with permission from Ref. (Guan et al., 2020). Copyright 2020 Elsevier.

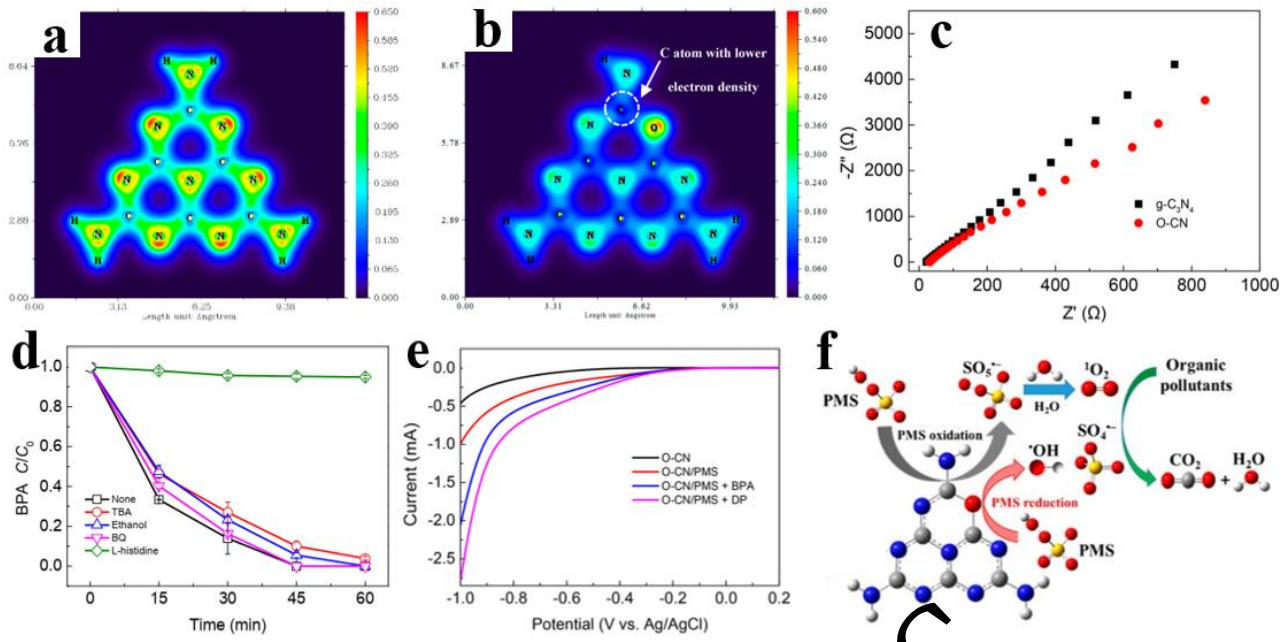

Fig. 7. Two-dimensional valence-electron density color-filled maps of (a) g-C_3N_4 and (b) O-CN. (c) EIS spectra of g-C_3N_4 and O-CN. (d) Effect of scavengers on catalytic degradation of BPA in the O-CN/PMS system. (e) LSV curves of O-CN with and without PMS and BPA or DP. (f) Mechanism of PMS activation by O-CN. Reproduced with permission from Ref. (Gao et al., 2018b). Copyright 2018 American Chemical Society.

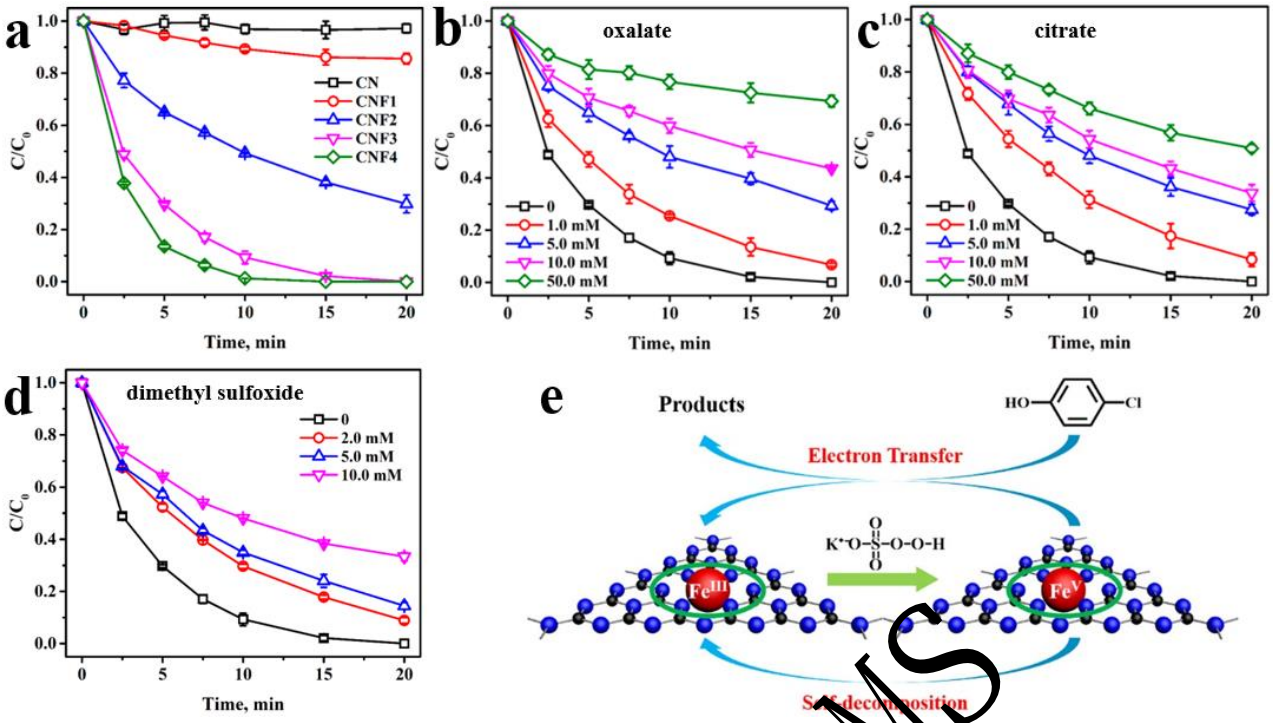

Fig. 8. (a) Degradation of 4-CP in different PMS/Fe(III)-g-C_3N_4 systems. Effects of (b) oxalate and (c) citrate on 4-CP degradation in the PMS/Fe(III)-g-C_3N_4 system. (d) Effect of DMSO on 4-CP degradation in the PMS/Fe(III)-g-C_3N_4 system. (e) Mechanism of PMS activation by Fe(III)-g-C_3N_4. Reproduced with permission from Ref. (Li et al., 2018). Copyright 2018 American Chemical Society.

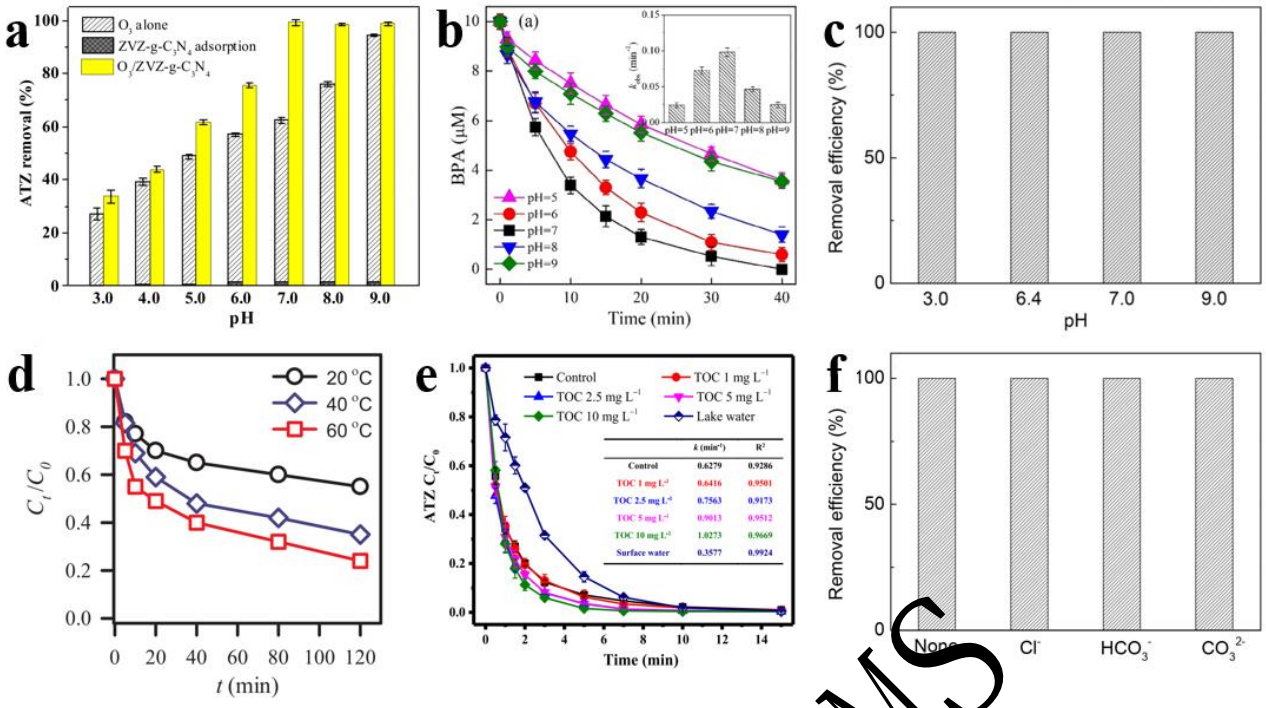

Fig. 9. (a) Effect of solution pH on the degradation of ATZ in the ZVZ-g-C_3N_4/O_3 system. Reproduced with permission from Ref. (Yuan et al., 2018b). Copyright 2018 Elsevier. (b) Effect of solution pH on the degradation of BPA in the g-C_3N_4-Melamine/PMS system. Reproduced with permission from Ref. (Guan et al., 2020). Copyright 2020 Elsevier. Effect of (c) solution pH and (f) common inorganic anions on the degradation of BPA in the O-CN/PMS system. Reproduced with permission from Ref. (Gao et al., 2018b). Copyright 2018 American Chemical Society. (d) Effect of temperature on the degradation of RhB in the S-g-C_3N_4/PDS system. Reproduced with permission from Ref. (Lin et al., 2018b). Copyright 2018 Elsevier. (e) Effect of NOM on the degradation of ATZ in the O@g-C_3N_4/O_3 system. Reproduced with permission from Ref. (Yuan et al., 2019). Copyright 2019 Elsevier.

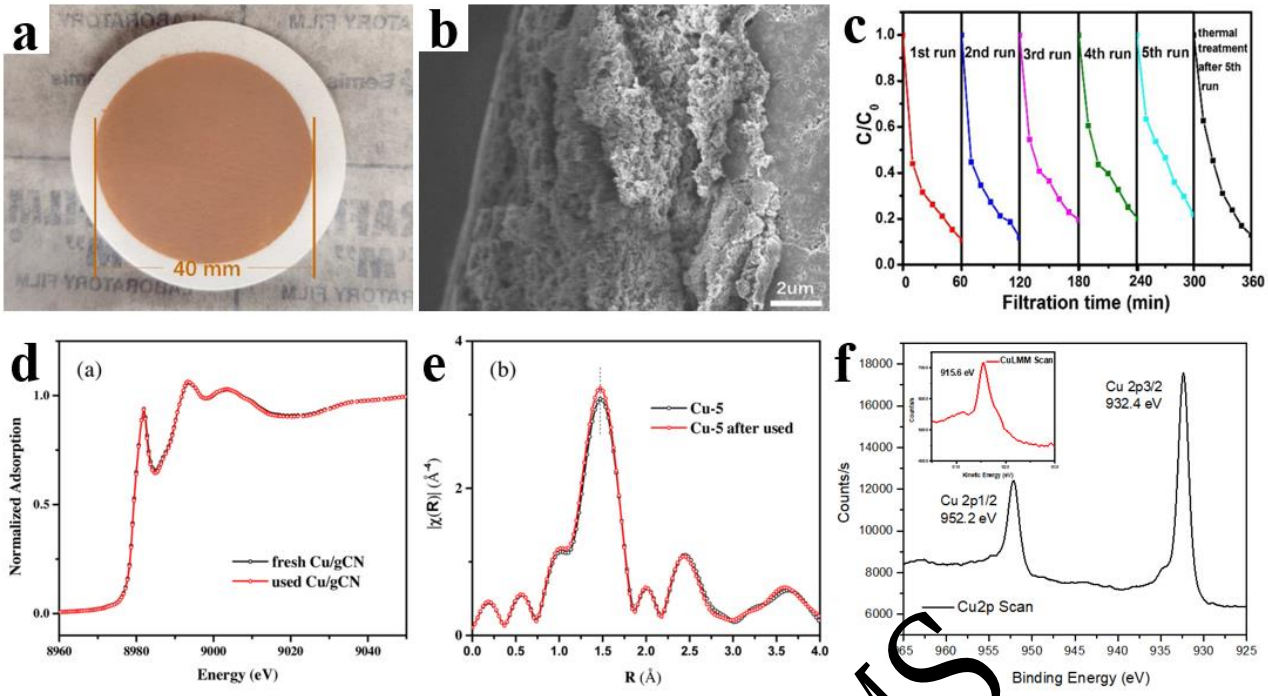

Fig. 10. (a) The digital image and (b) cross-sectional SEM of Mn_3O_4/g-C_3N_4@PTFE membrane. (c) The reusability of Mn_3O_4/g-C_3N_4@PTFE membrane for 4-CP degradation in the presence of PMS. Reproduced with permission from Ref. (Chen et al., 2020a). Copyright 2020 Elsevier. The comparison of (d) XANES and (e) EXAFS spectra at the Cu K-edge between the fresh Cu(I)-g-C_3N_4 and the catalyst after the degradation reaction. (f) XPS spectra of Cu 2p and Cu LMM Auger electron spectra (insert graph) of the used Cu(I)-g-C_3N_4. Reproduced with permission from Ref. (Ma et al., 2019b). Copyright 2019 Elsevier.